

AEROELASTIC MODELING AND ANALYSIS OF HIGH ASPECT RATIO
WINGS WITH DIFFERENT FIDELITY STRUCTURAL MODELS

A THESIS SUBMITTED TO
THE GRADUATE SCHOOL OF NATURAL AND APPLIED SCIENCES
OF
MIDDLE EAST TECHNICAL UNIVERSITY

BY

GÖKÇEN ÇİÇEK

IN PARTIAL FULFILLMENT OF THE REQUIREMENTS
FOR
THE DEGREE OF MASTER OF SCIENCE
IN
AEROSPACE ENGINEERING

DECEMBER 2019

Approval of the thesis:

**AEROELASTIC MODELING AND ANALYSIS OF HIGH ASPECT RATIO
WINGS WITH DIFFERENT FIDELITY STRUCTURAL MODELS**

submitted by **GÖKÇEN ÇİÇEK** in partial fulfillment of the requirements for the degree of **Master of Science in Aerospace Engineering Department, Middle East Technical University** by,

Prof. Dr. Halil Kalıpçılar
Dean, Graduate School of **Natural and Applied Sciences**

Prof. Dr. İsmail Hakkı Tuncer
Head of Department, **Aerospace Engineering**

Prof. Dr. Altan Kayran
Supervisor, **Aerospace Engineering, METU**

Examining Committee Members:

Prof. Dr. Dilek Funda Kurtuluş
Aerospace Engineering, METU

Prof. Dr. Altan Kayran
Aerospace Engineering, METU

Prof. Dr. Demirkan Çöker
Aerospace Engineering, METU

Assoc. Prof. Dr. Nilay Sezer Uzol
Aerospace Engineering, METU

Assist. Prof. Dr. Touraj Farsadi
Aerospace Engineering, Adana Sci. and Tech. Uni.

Date: 10.12.2019

I hereby declare that all information in this document has been obtained and presented in accordance with academic rules and ethical conduct. I also declare that, as required by these rules and conduct, I have fully cited and referenced all material and results that are not original to this work.

Name, Surname: Gökçen Çiçek

Signature:

ABSTRACT

AEROELASTIC MODELING AND ANALYSIS OF HIGH ASPECT RATIO WINGS WITH DIFFERENT FIDELITY STRUCTURAL MODELS

Çiçek, Gökçen
Master of Science, Aerospace Engineering
Supervisor: Prof. Dr. Altan Kayran

December 2019, 86 pages

The focus of this study is in the area of static aeroelasticity, and it is concerned with modeling and analysis of high aspect ratio wings experiencing large torsional deflections. In this study, the effects of different fidelity structural models on static aeroelasticity are investigated. Preference of light and flexible structures due to performance and weight criteria and certification requirements make the aeroelastic analysis more and more essential for aircraft. Especially for the preliminary design phase, simple models are preferred to reduce the computational time and to perform the design iterations. Such a study is important in order to obtain aeroelastically efficient structure and integrate aeroelastic concepts at the preliminary design stage without making analysis complicated. The research approach adopted in this thesis includes loosely coupled structural and aerodynamic models. The approach for the structural modeling presented here is based on both linear and nonlinear structural theories. The linear structural theory is based on bending-torsion beam finite element formulations. The nonlinear theory is based on the nonlinear finite element model with only torsional rotation degree of freedom to study specifically the static aeroelastic behavior. The aerodynamic theories used for the aeroelastic coupling are lifting line theory and lifting surface theory which is based on Multhopp-Richardson's solution to provide the spanwise loading of lifting surfaces with camber and twist. The focus

of the thesis study is on divergence, one of the most important aeroelastic phenomenon. Analyses are performed by coupling the two different structural models with the lifting line theory and lifting surface theory to perform the divergence analysis of a simple plate-like wing model. Significant differences are observed between the linear and the nonlinear solution methodologies in terms of torsional deflection of the tip of the wing. The linear theory is found to be conservative with respect to the nonlinear theory for high aspect ratio wings. The findings from this research provide evidence that for more realistic calculation of divergence instability of high aspect ratio wings, geometric nonlinearity should be taken into consideration. This thesis recommends a comparison of solutions for different types of wing models in order to better understand the accuracy of each method.

Keywords: Nonlinear Static Aeroelasticity, Computational Aeroelasticity, Finite Element Method, Nonlinear Torsion, Coupled Solution, Strip Theory, Lifting Surface Theory, Potential Theory, High Aspect-Ratio Wings

ÖZ

YÜKSEK EN-BOY ORANINA SAHİP KANATLAR İÇİN FARKLI DOĞRULUKTAKİ YAPISAL MODELLERLE AEROELASTİK ANALİZ VE MODELLEME

Çiçek, Gökçen
Yüksek Lisans, Havacılık ve Uzay Mühendisliği
Tez Danışmanı: Prof. Dr. Altan Kayran

Aralık 2019, 86 sayfa

Bu çalışma statik aeroelastisite alanındadır ve yüksek en-boy oranlı kanatların modellenmesi ve analizi ile ilgilidir. Bu çalışmada, farklı doğruluktaki yapısal modellerinin aeroelastik analizler üzerindeki etkileri araştırılmıştır. Performans ve ağırlık kriterleri ve sertifikasyon gereklilikleri nedeniyle hafif ve esnek yapıların tercih edilmesi, aeroelastik analizleri uçaklar için giderek daha önemli hale getirmektedir. Özellikle ön tasarım aşamasında, hesaplama süresini azaltmak ve tasarım değişikliklerini gerçekleştirmek için basit modeller tercih edilir. Böyle bir çalışma, aeroelastik olarak etkin bir yapı elde etmek ve aeroelastik analizleri karmaşık hale getirmeden ön tasarım aşamasında fikir edinebilmek için önemlidir. Bu tezde benimsenen araştırma yaklaşımı gevşek bağlı yapısal ve aerodinamik modelleri içermektedir. Burada sunulan yapısal modelleme yaklaşımı hem doğrusal hem de doğrusal olmayan yapısal teorilere dayanmaktadır. Doğrusal yapısal teori, bükülme burulmalı kiriş sonlu elemanlar formülasyonlarına dayanmaktadır. Doğrusal olmayan teori, özellikle statik aeroelastik davranışı incelemek için sadece burulma rotasyon serbestlik derecesine sahip doğrusal olmayan sonlu eleman modeline dayanmaktadır. Aeroelastik bağlama için kullanılan aerodinamik teoriler şerit teorisi ve Multhopp-Richardson'un çözümüne dayanan kaldırma yüzeyi teorisidir. Tez çalışmasının odak

noktası, en önemli aeroelastik olgulardan biri olan ıraksama üzerinedir. Basit bir plaka benzeri kanat modelinin ıraksama analizini yapmak için iki farklı yapısal modelin şerit teorisi ve kaldırma yüzeyi teorisi ile birleştirilmesiyle analizler gerçekleştirilir. Doğrusal ve doğrusal olmayan çözüm metodolojileri arasında kanadın ucunun burulma açısı göz önüne alındığında önemli farklılıklar gözlenir. Doğrusal teorinin, yüksek en-boy oranlı kanatlar için doğrusal olmayan teoriye göre konservatif olduğu bulunmuştur. Bu araştırmadan elde edilen bulgular, yüksek en-boy oranlı kanatların ıraksama kararsızlığının daha gerçekçi bir şekilde hesaplanması için geometrik doğrusalsızlığın önemini vurgular. Bu tez, her yöntemin doğruluğunu daha iyi anlamak için farklı kanat modelleri için çözümlerin karşılaştırılmasını önerir.

Anahtar Kelimeler: Doğrusal Olmayan Statik Aeroelastisite, Hesaplamalı Aeroelastisite, Sonlu Elemanlar Yöntemi, Doğrusal Olmayan Burulma, Şerit Teorisi, Kaldırma Yüzeyi Teorisi, Potansiyel Teori, Yüksek En-Boy Oranlı Kanatlar

To the love of my life

ACKNOWLEDGEMENTS

First and foremost, I would like to thank my supervisor Prof. Dr. Altan Kayran for his guidance and support.

I would like to thank to the members of my thesis committee: Prof Dr. Funda Kurtuluş, Prof. Dr. Demirkan Çöker, Assoc. Prof. Dr. Nilay Sezer Uzol and Assist. Prof. Dr. Touraj Farsadi for their valuable and effective comments.

I want to thank my father for making me feel he is always there for me and my mother for being with me all the time with her heart and soul.

I want to express my appreciation to my grandparents for taking care of me; my grandmother for her unconditional love and my grandfather for teaching me how to smile.

I would like to express my deepest gratitude to the love of my life, Orhun Çiçek for bringing joy and happiness to my life. I would not have completed without his support.

I want to thank Esra Balcı for her support and love and all of my friends for bringing me happiness.

I want to dedicate this thesis for a better world.

TABLE OF CONTENTS

ABSTRACT	v
ÖZ	vii
ACKNOWLEDGEMENTS	x
TABLE OF CONTENTS	xi
LIST OF TABLES	xv
LIST OF FIGURES	xvii
LIST OF SYMBOLS	xix
CHAPTERS	
1. INTRODUCTION	1
1.1. Definition of Divergence Phenomena	1
1.2. Scope and Delimitations of Thesis	2
1.3. Background Information and Literature Survey	3
1.3.1. History of Aeroelasticity	3
1.3.2. Background Information on Computational Aeroelasticity	4
1.3.3. Field of Fluid-Structure Interaction	5
1.3.4. Current Modeling Methods for High Aspect-Ratio Wings in Terms of Nonlinear Static Aeroelasticity.....	7
1.3.5. State-of-Art and Literature Survey for Nonlinear Static Aeroelasticity	9
1.4. Previous Studies in METU on Static Aeroelasticity	11
1.5. Motivation of Thesis.....	13
1.6. Research Objectives	13
1.7. Outline of Thesis	14

2.	AERODYNAMIC MODELS.....	17
2.1.	Strip Theory (Lifting Line Theory)	17
2.1.1.	Continuous Wing	17
2.1.2.	Discretized Wing.....	19
2.2.	ESDUpac A9510	20
2.2.1.	Multhopp-Richardson’s Solution.....	20
2.3.	Doublet-Lattice Method.....	21
3.	STRUCTURAL MODELS	25
3.1.	Linear Structural Models	25
3.1.1.	Bending-Torsion Beam Finite Element Model.....	25
3.1.1.1.	The Euler-Bernoulli Beam Theory	26
3.1.1.2.	Torsion Bar.....	28
3.1.1.3.	Combined Model	29
3.2.	Nonlinear Torsion Beam Finite Element Model	32
3.2.1.	Overview	32
3.2.2.	Solution Procedure.....	34
3.2.3.	Lagrangian Formulation	37
3.2.4.	Derivation of Nonlinear Equations	38
3.2.5.	Nonlinear Elastic Nonuniform Torsion Beam	47
3.2.	Nonlinear Torsion Beam Finite Element Model	32
4.	STATIC AEROELASTIC MODELS.....	51
4.1.	Bending-Torsion Beam Finite Element based Aeroelastic Model (Model 1 & Model 2)	51
4.2.	Nonlinear Torsion Beam Finite Element based Aeroelastic Model (Model 3 & Model 4)	53

4.3. NASTRAN Verification Model with SOL144	54
5. RESULTS	57
5.1. Patil-Hodges Wing	57
5.2. Structural Model Verifications	60
5.2.1. Bending-Torsion Beam FEM Verification	61
5.2.1.1. Concentrated Load Case	61
5.2.1.2. Distributed Load Case.....	63
5.2.2. Nonlinear Torsion Beam FEM Verification	65
5.2.2.1. Concentrated Load Case	66
5.2.2.2. Distributed Load Case.....	67
5.3. Comparison of Structural Models	67
5.3.1. Vertical Displacement Results Comparison of Structural Models	68
5.3.2. Bending Rotation Angle Results Comparison of Structural Models	69
5.3.3. Twist Angle Results Comparison of Structural Models.....	71
5.4. Comparison of Aeroelastic Models	73
5.4.1. Analysis of High Aspect Ratio Wings	74
5.4.2. Analysis of Low Aspect Ratio Wing Model	76
5.5. Case Studies	77
5.5.1. Aspect Ratio Effect on the Divergence Speed.....	77
5.5.2. Bending Rigidity Effect on the Divergence Speed	78
5.5.3. Torsional Rigidity Effect on the Divergence Speed	78
6. CONCLUSION	79
REFERENCES	81

LIST OF TABLES

TABLES

Table 1.1. Outline of the Aeroelastic Models	14
Table 5.1. Design Parameters of Patil-Hodges Wing [24] [25] [61]	58
Table 5.2. Flight Conditions of Patil-Hodges Wing [24] [25] [61]	58
Table 5.3. Shell model orthotropic material properties	59
Table 5.4. Comparison of linear frequency results (Hz) of shell model with the test case [24]	60
Table 5.5. Linear shell model verification for the vertical tip displacement: concentrated load case	62
Table 5.6. Bending-torsion beam structural model verification for the vertical displacement and bending rotation: concentrated load case	63
Table 5.7. Pitching moment vs elastic tip twist angle for the bending-torsion beam: concentrated load case	63
Table 5.8. Pitching moment vs elastic tip twist angle for the bending-torsion beam: concentrated load case	64
Table 5.9. Bending-torsion beam structural model verification for the elastic tip twist angle: distributed load case	65
Table 5.10. Nonlinear shell model verification for the vertical tip displacement: concentrated load case	66
Table 5.11. Tip twist vs force for the nonlinear torsion beam: concentrated load case	67
Table 5.12. Nonlinear torsion beam structural model verification for the tip twist angle: distributed load case	67
Table 5.13. Vertical displacement vs force: distributed load case	68
Table 5.14. Bending rotation vs force: distributed load case	70
Table 5.15. Tip twist angle vs pitching moment: distributed load case.....	72

Table 5.16. Comparison of divergence speed results of aeroelastic methods for high aspect ratio wing model	74
Table 5.17. Comparison of divergence speed results of aeroelastic methods for low aspect ratio wing model	76
Table 5.18. Aspect ratio effect on the divergence speed	77
Table 5.19. Sensitivity of divergence speed with respect to EI	78
Table 5.20. Sensitivity of divergence speed with respect to GJ	78

LIST OF FIGURES

FIGURES

Figure 1.1. Geometry of Typical Section Airfoil [2]	1
Figure 1.2. Elastic Twist versus Airspeed [2]	2
Figure 1.3. Aerodynamic models used in aeroelastic calculations [12]	5
Figure 1.4. Structural models used in aeroelastic calculations [12]	5
Figure 2.1. Aerodynamic strip on a continuous wing [45]	17
Figure 2.2. Dimensions of a rectangular wing [45]	18
Figure 2.3. Aerodynamic Strips on a discretized rectangular wing [45]	19
Figure 2.4. Doublet-Lattice Panel Subdivided into Boxes [49]	22
Figure 3.1. Two-node beam bending element	26
Figure 3.2. Shape functions for a two-node beam element	27
Figure 3.3. Nodal forces for a two-node beam element	27
Figure 3.4. Two-node torsion element	29
Figure 3.5. Combined bending-torsion beam element [45]	29
Figure 3.6. Two node beam element	30
Figure 3.7. Deformation of a beam under a couple	33
Figure 3.8. Nonlinearities in solid mechanics	33
Figure 3.9. Initial/undeformed and the current/deformed states of structure [54]	38
Figure 3.10. Coordinate system of a thin-walled l-beam [55]	39
Figure 3.11. Transverse displacements of the cross-section [55]	40
Figure 4.1. Iterative process of Model 1 & Model 2	52
Figure 4.2. Iterative process of Model 3 and Model 4	54
Figure 4.3. Flowchart of SOL144	56
Figure 5.1. Patil-Hodges wing [32]	57
Figure 5.2. Structural Model of Patil-Hodges Wing	58
Figure 5.3. Mode shapes of the shell model	60

Figure 5.4. Vertical tip force application on the shell model	61
Figure 5.5. Pitching moment application at the tip location of the shell model	62
Figure 5.6. Distributed vertical load application on the shell model	64
Figure 5.7. Distributed pitching moment application on the shell model	65
Figure 5.8. Spanwise vertical displacement of the wing: comparison of linear and nonlinear results under 1 N/m distributed vertical loading	68
Figure 5.9. Spanwise vertical displacement of the wing: comparison of linear and nonlinear results under 10 N/m distributed vertical loading	69
Figure 5.10. Spanwise vertical displacement of the wing: comparison of linear and nonlinear results under 20 N/m distributed vertical loading	69
Figure 5.11. Spanwise bending rotation of the wing: comparison of linear and nonlinear results under 1 N/m distributed vertical loading	70
Figure 5.12. Spanwise bending rotation of the wing: comparison of linear and nonlinear results under 10 N/m distributed vertical loading	71
Figure 5.13. Spanwise bending rotation of the wing: comparison of linear and nonlinear results under 20 N/m distributed vertical loading	71
Figure 5.14. Spanwise twist rotation of the wing: comparison of linear and nonlinear results under 10 N distributed pitching moment	72
Figure 5.15. Spanwise twist rotation of the wing: comparison of linear and nonlinear results under 50 N distributed pitching moment	73
Figure 5.16. Spanwise twist rotation of the wing: comparison of linear and nonlinear results under 100 N distributed pitching moment	73
Figure 5.17. Elastic twist angle of Cooper's at 32.5m/s [33]	75
Figure 5.18. Elastic twist of developed FE models at 32.5m/s	75
Figure 5.19. Comparison of linear and nonlinear method results of stable aeroelastic deformation	77

LIST OF SYMBOLS

SYMBOLS

α_e	Elastic twist angle
a_w	Effective lift curve slope
a_0	2D airfoil lift curve slope
b	Half span of the wing
c	Chord of the wing
EI	Bending rigidity
GJ	Torsional rigidity
I_n	Nonlinear Wagner constant
I_w	Warping section constant
J	Torsion section constant
L	Length of the half span
M_z	Torque at a distance z along the torsion member
t	Thickness of the wing
V	Free stream velocity
y	Spanwise displacement of the wing
z	Transverse displacement of the wing for linear structure model
z	Longitudinal axis through centroid for nonlinear structure model
$[B_L], [B_Q]$	Matrices for linear and quadratic strains
$[CI]$	Matrix for nodal deformations
$[D]$	Tangent modulus constitutive matrix
$\{e\}$	Vector of equilibrium equation errors
$\{F_E\}$	Vector of external applied actions
$\{F_I\}$	Vector of equivalent internal resistances
$[K_T]$	Tangent stiffness matrix
$[K_L]$	Small displacement component of tangent stiffness matrix
$[K_Q]$	Large displacement component of tangent stiffness matrix
$[K_\sigma]$	Geometric component of tangent stiffness matrix
$[M_\sigma]$	Geometric matrix
$[N_e]$	Element shape function
$[N]$	Matrix relating $\{u, v, w, \phi\}^T$ to $\{\delta\}$
$[N_\sigma]$	Matrix relating $\{\phi\}$ to $\{\delta\}$
$\{r_e\}$	Consistent load vector
$\{Z\}$	Vector of powers of z/L
$\{\delta_\phi\}$	Vector of nodal deformations
$\{\Delta\delta_\phi\}$	Vector of nodal deformation increments
Φ	Twist rotation
$\{\sigma\}$	Generalized stress resultants

CHAPTER 1

INTRODUCTION

1.1. Definition of Divergence Phenomena

Static aeroelasticity is the field that concentrates on the interaction between steady flows induced aerodynamic loads and the resultant elastic deformation of the wing structure. The nature of this phenomenon is time-independent, that is to say it is insensitive to the rate and acceleration of structural deflections. In this area, there are two common design problems. First one is the effect of elastic deformations on the flight loads related to the normal operating conditions. This effect has significant impact on aircraft performance, handling qualities, stability of flight, and load distribution on the wing. Secondly, the risk of static instability of the structure can lead to catastrophic failure which is called as divergence [1].

Typical section model is appropriate for comprehending the philosophy of divergence phenomenon. In Figure 1.1, a simplified aeroelastic model is demonstrated. The wing is modeled as flat plate mounted at its elastic axis with a torsional spring. The main focus on this model is the rotation of the plate α as a function of the free stream velocity U . If the stiffness of the spring is small or the velocity of the freestream is high, the rotation of the plate may go beyond its torsional resistance which results in structural failure.

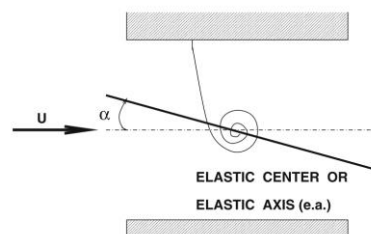


Figure 1.1. Geometry of Typical Section Airfoil [2]

The velocity-dependent change of the elastic twist angle of the plate is pointed out in Figure 1.2. Structural failure occurs at divergence speed where the twist angle becomes infinite. Any theoretical static aeroelastic models aim to estimate the actual divergence speed, U_D of the wing. This graphical representation is valid for all types of real aircraft wings [2].

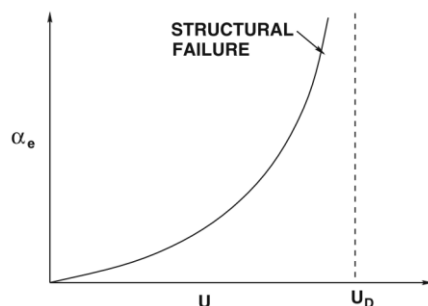


Figure 1.2. Elastic Twist versus Airspeed [2]

1.2. Scope and Delimitations of Thesis

The scope of the thesis with delimitations are listed below.

- This study focuses on the aeroelastic modeling of the fixed wings. For simplicity, the modeling approach is based on the usage of simple plate model.
- Different fidelity structural models are developed and coupled with lifting line theory and lifting surface theory.
- The approach for structural modeling presented in this thesis is derived from the linear and the nonlinear theories. The linear theory is based on bending-torsion beam finite element formulation. The nonlinear model is based on the nonlinear finite element model, in which only torsional freedom is modeled as nonlinear.
- Bending-torsion degrees of freedoms are uncoupled.
- High aspect ratio wing has large deformations that require the inclusion of geometric nonlinearity in the equation. Therefore, the impact of nonlinearity

on the aeroelastic model is investigated for high aspect ratio wings and compared with the results of linear models.

- Material nonlinearity is out of the scope of this thesis.
- Analyses are performed for static conditions, i.e. there is no time dependency.

1.3. Background Information and Literature Survey

1.3.1. History of Aeroelasticity

Aeroelasticity concerns the mutual interaction of aerodynamic, elastic and inertial forces. Static aeroelasticity arises from the interaction of aerodynamic and inertial forces, on the other hand, all of the forces are necessary to compose dynamic aeroelastic behavior.

Historical review on aeroelasticity and its impact on aircraft design were overviewed by Collar [3]. Friedmann demonstrated the importance of aeroelasticity in aircraft design [4]. Dowell et al. [5] emphasized recent developments and future challenges in modeling of fluid-structure interaction. Livne presented an overview on various perspectives of the fixed wing aeroelasticity [6]. Main challenges in aeroelasticity was demonstrated by Bendiksen [7]. Livne and Weisshaar reviewed the history of nonconventional aircrafts to constitute aeroelastic effects as design qualification and analyzed the potential effect of experiences on current aircraft configurations [8]. Especially new theoretical methods were discussed in detail. Schuster et al. [9] examined the development and implementation of aeroelastic methods. Bhatia presented a perspective on the aeroelasticity related topics [10]. Xiang et al. [11] presented the recent advance in nonlinear aeroelasticity. Recently, a comprehensive review on nonlinear aeroelasticity of high aspect-ratio wings was performed by Afonso et al. [12].

1.3.2. Background Information on Computational Aeroelasticity

Computational Aeroelasticity is constituted from the coupling of Computational Fluid Dynamics tools with Computational Structural Dynamics methods to implement aeroelastic analysis [9]. Recently, in non-linear aeroelasticity, the fidelity and coupling of structural and aerodynamic models has changed dramatically. Some of the factors affecting model selection are listed below [12].

- The nonlinearity types in structural and aerodynamic models
- Required computational time
- Required accuracy
- Phase of the project (preliminary design phase, critical design phase, certification phase)
- Eligibility of the study (academic, validation of models)
- Cost of the development (in terms of engineering effort) [13]

In preliminary design phase, low to medium fidelity analysis tools are preferred by reasons of being convenient for optimization process and having fast feedback in the decision process. The advantages of these tools minimize the long-term costs of the projects.

For more realistic modeling to capture physical nature of the problem, high fidelity models are required. These models are appropriate for advanced phases of the project to optimize the design model and to specify the critical test models for the verification of the results and elimination of the uncertainties of the analysis model [12].

Aerodynamic and structural models commonly used in the aeroelastic analysis are demonstrated in Figure 1.3 and Figure 1.4.

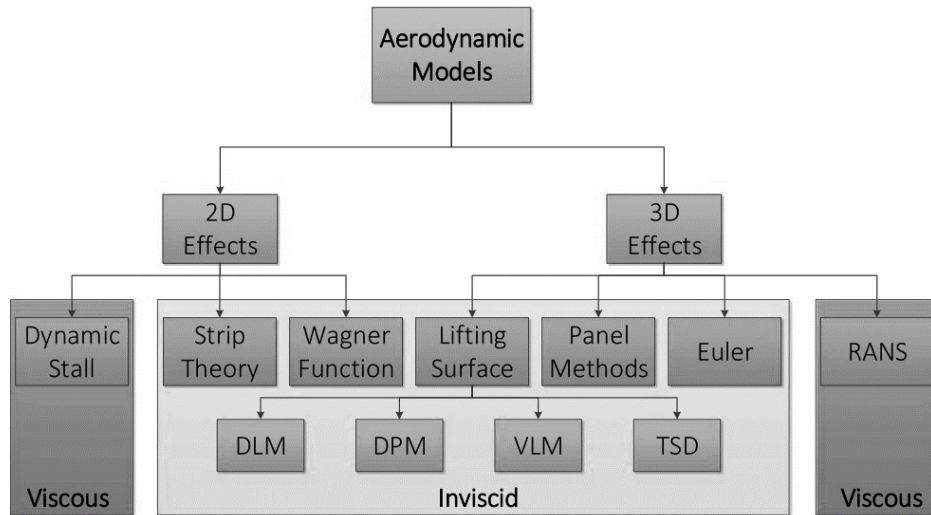


Figure 1.3. Aerodynamic models used in aeroelastic calculations [12]

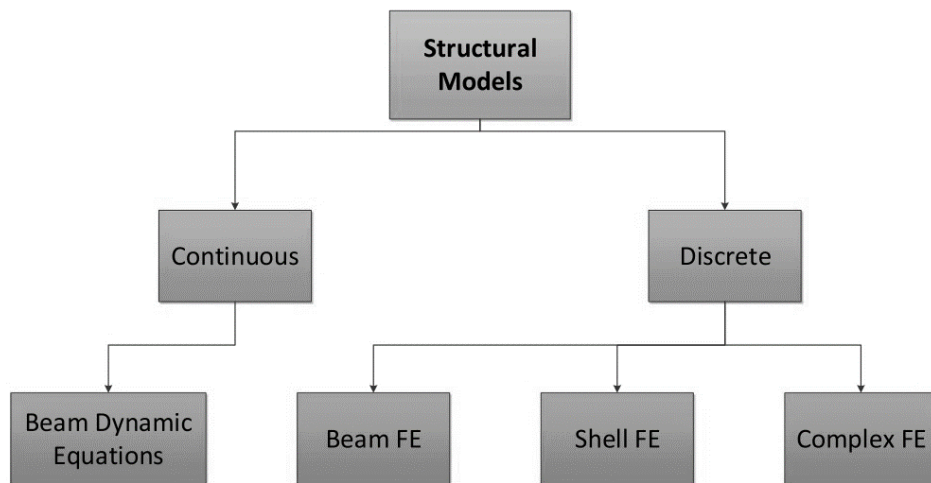


Figure 1.4. Structural models used in aeroelastic calculations [12]

1.3.3. Field of Fluid-Structure Interaction

For the aeroelastic analysis, the solution of the structural and aerodynamic methods are generally carried out separately. There are separate solvers for each of the disciplines in addition countless number of coupling methods. Moreover, the fully-coupled models are available for the solution process for instance Direct Method.

However, they are not preferred in the industry because of obligation to work of different compartments simultaneously [12].

The data transfer between structural and aerodynamic models is essential to transfer necessary information from one domain to another. Therefore, for the coupling of the models, the convergence criteria should be met between structural and aerodynamic models. The coupling between models must guarantee conservation, coherence and shape preservation [14].

The FSI solvers can be categorized according to the data transfer types [12]:

- Partitioned: The convergence of structural and aerodynamic models is performed individually.
- Monolithic: The convergence criteria is valid for the coupled model.
- Mixed: The convergence criteria depend on the order of representations of the system. It will be either partitioned or monolithic based on the necessity of the representation order.

Bazievs et al. [15] state that FSI methods for coupled equations can be handled in two approaches which are strongly-coupled and loosely-coupled. For the former method, solution is performed simultaneously whereas in the latter aerodynamic and structural equations are solved separately and coupled afterwards. The solution procedure is iterated until the convergence criteria is satisfied.

Kamakoti and Shyy [16] emphasized that strongly-coupled equations have limitations on mesh densities due to high computational cost. Besides, loosely-coupled approach is restricted with small perturbations and reasonable nonlinearities. Nevertheless, Bazievs et al. [15] highlighted that loosely-coupled FSI is frequently preferred and ensures high accuracy results for nonlinear problems. They also demonstrated the formulations of loosely-coupled methods in detail for both static and dynamic aeroelasticity problems. Kamakoti and Shyy [16] demonstrated aerodynamic, structural and interface methods schematically according to different fidelities.

Nonlinear aeroelastic phenomena prediction was introduced for industrial aircrafts by Henshaw et al. [14]. The main focus of this survey is FSI methods. The difficulties in the coupling of aerodynamic and structural models were explained and various solution methodologies were negotiated.

Hallissy and Cesnik [17] indicated that the flutter speed obtained by strongly-coupled methods are 2-5% higher than lower-order models. They used beam formulation as structural model to catch local effects on deformations. For the aerodynamic model, Euler/RANS method was preferred. Partitioned FSI was performed.

Mian et al. [18] built up FSI solution methodology to review the effect of nonlinearity on high-aspect ratio wings. The method was a combination of a partitioned model which is composed of finite element solver and RANS. The results were validated with the experimental results of Tang and Dowell [19]. Linear and nonlinear FSI solutions were compared and comparison results showed the importance of considering geometric nonlinearities.

1.3.4. Current Modeling Methods for High Aspect-Ratio Wings in Terms of Nonlinear Static Aeroelasticity

Low fidelity models are preferred for the nonlinear aeroelastic analysis of high aspect-ratio wings. The studies performed in this area have a great deal of similarities. Generally, low-subsonic speeds are preferred, beam with large deformation constitutes structural model and 2D quasi-static aerodynamic models are selected. The beam models are isotropic with constant cross-section along the span, in general [12].

In 1992, Dunn and Dugundji [20] analyzed aeroelastic behavior of an 8.7 aspect-ratio rectangular wings with different bending-torsion stiffness characteristics. Nonlinear aeroelastic analysis was performed by the coupled model of Rayleigh-Ritz method and nonlinear stall aerodynamic model called ONERA. Newton Raphson method was used as the solution methodology. The results of the analysis were compared with experimental data obtained from the strain gages of bending and torsion.

Patil et al. [21] presented the nonlinear aeroelastic results for a wing with semi-span aspect-ratio of 16. The steady aerodynamic modeling effects were evaluated. The extended version of this study [22] considered the subsonic, unsteady flow, tendency to dynamic stall, material anisotropy and geometric nonlinearity. Linear results were verified for the Goland Wing [23], moreover, further results were achieved which demonstrated the nonlinearity effects on structural and aerodynamic models.

Patil et al. [24] performed a study related to a wing with aspect-ratio of 36. The study demonstrated the results for the flutter velocity as in consequence of linear models and according to results it was realized that when the tip displacement increased, flutter velocity was decreased.

Patil and Hodges [25] reviewed the significance of nonlinearity for structural and aerodynamic models. Their structural model depended on improved Hodges formulation, and for the steady aerodynamics Vortex-Lattice method (VLM) was used and DLM was chosen for the unsteady part. In this study, the aerodynamic loading was compared for a deformed rigid wing with constant angle of attack and for a wing with constant angle of attack at the root. In the former case, non-planar aerodynamic effects were negligible, however in the latter case, torsional deformation of the wing affected the aerodynamic loading considerably.

Xie et al. [26] performed flutter analysis for a composite high aspect-ratio wing by the coupled model of nonlinear beam finite element and DLM. Moreover, nonlinear static equilibrium state was determined with design loads regarding follower force effects. This work emphasized that nonlinear modeling for aeroelastic analysis is crucial in the design stages.

Tang et al. [27] built up a new wind tunnel test model to investigate the gust response on a high aspect ratio wing at low subsonic speeds. Nonlinear beam theory was used as structural model and coupled with ONERA aerodynamic model. The aeroelastic model was comprised of a wing with 18 aspect-ratio and NACA0012 airfoil. In the analyses, flexible support system effects of the wing, the static aeroelastic root

displacement, nonlinear flutter and gust responses were investigated. The analyses results indicated good correlation with the test data.

1.3.5. State-of-Art and Literature Survey for Nonlinear Static Aeroelasticity

Xie et al. [28] presented an experimental study by resampling similar approach with Tang and Dowel [19]. For the modeling of static aeroelasticity, finite element model coupled lifting line theory was preferred. The displacement results were compared for the linear and nonlinear models, and then verified with the experiment results. It was concluded that the lifting line theory was appropriate for static aeroelasticity modeling of an aircraft at the preliminary design phase.

Harmin and Cooper [29] reported practical reduced order aeroelastic models for wings exposed to geometric nonlinearities. Combined modal/finite element [30] was implemented as methodological approach. Doublet lattice method (potential theory) was used as aerodynamic method to constitute a reduced order model estimating flexible wing aeroelastic response. This method was carried out for designating gust response and static aeroelastic deflection.

Huixue et al. [31] conducted nonlinear aeroelastic analysis for high-aspect ratio wings with large geometrical deformation. A loosely-coupled CFD/CSD method was implemented as an aeroelastic solver. Structural and aerodynamic loops were solved individually with an exchange of variables supplying fluid-structure interface. Nonlinear CSD method was coupled with an unsteady Euler solver. The interface method was a fully three-dimensional integral constant volume tetrahedron technique. The computational time of the method was reduced by the golden section method which accelerated convergence. Wing structure was modeled by both linear and nonlinear theories. It was demonstrated that geometric nonlinearity was crucial for static aeroelasticity analysis of high aspect-ratio flexible wings.

Howcroft et al. [32] elaborated five different aeroelastic models to examine a high aspect-ratio wing under excessive structural deformations. The wing modeled in this

paper was based on the study of Patil et al. [24]. Each method was evaluated separately, and the results were compared. As a result of all methods, it had been concluded that the orientation of aerodynamic forces had a significant effect on the consistency between predicted loads and displacements. Differences arising from linear modeling of the wing were also presented and discussed. It was obtained that over-estimated wing deflection, aerodynamic forces and root bending moment were caused by linearization.

Castelliani et al. [33] presented two methods for the nonlinear aeroelastic analysis of high aspect ratio wings. The two methods were the nonlinear finite element and multibody dynamics. The structural models of the two methods were coupled with the doublet lattice method (potential theory) and strip theory (lifting line theory), respectively. The results of the static aeroelastic analyses were demonstrated and compared with the linear analysis in terms of internal loads at trim conditions. As a conclusion, it was pointed out that follower force effect and geometrical nonlinearity had a great influence on the differences between linear and nonlinear aeroelastic models. The linear and nonlinear results were validated with the test case for flexible high aspect-ratio wing presented by Patil et al. [24].

Lan et al. [34] implemented a nonlinear static aeroelastic analysis depending on CFD/CSD coupling methodology. The loosely coupled solution was approached by a conventional serial staggered procedure. The Reynolds-averaged Navier-Stokes equations were coupled with a geometrical nonlinear finite element method. The mesh structure was updated by the use of hybrid approach with rotation refinement. The analyses were performed with a high aspect-ratio wing and verified with wind tunnel test results.

Xie et al. [35] carried out a method for the high aspect ratio wings with geometric nonlinearity by reduced order model (ROM). ROM was preferred due to having low computational time. The structural model was based on the combined modal/finite element method which identified the stiffness nonlinearities. The non-planar vortex

lattice method was used to compute aerodynamic forces. Surface spline method is implemented for the coupling of structural and aerodynamic models. The method was solved for the static aeroelastic analysis and static aeroelastic trim configurations of the wings. The results demonstrated that a good agreement was achieved by static aeroelastic and trim analysis based on ROM with the finite element analysis and experiments.

Zhang et al. [36] performed static aeroelastic response and trim analyses for high aspect-ratio wings of a joined-wing aircraft. The methodology was based on the a geometrically nonlinear 3D corotational double-spar structural model coupled with a 3D nonplanar vortex lattice aerodynamic model. Inertia relief was utilized for the determination of the mass distribution effects on the static deformations. For the verification of the numerical model, a static structural test was conducted. Aeroelastic deformations, lift predictions and aerodynamic coefficients with their derivatives were analyzed in detail and compared for linear and nonlinear structural models.

Kantor et al. [37] derived a modal structural model coupled with a nonlinear aerodynamic model for static aeroelasticity analysis of flexible wing configurations. The geometrical nonlinearity was taken into consideration in structural model which calculates deformations of a beamlike structure by splitting the beam into several pieces. Large deflections were assumed to comprise of rigid and elastic deformations of the pieces. The difficulties encountered while applying a modal method were reported in the paper. An equivalent strip theory (lifting line theory) was implemented as aerodynamic model. The aeroelastic model was applicable for beam-like wing structures. The methodology was validated by three different load cases.

1.4. Previous Studies in METU on Static Aeroelasticity

In this section, previous studies published in METU on the topic of static aeroelasticity analysis of fixed wings are reviewed chronologically. Sümer improved in his thesis a 3-D Euler flow solver coupled with a finite element program to solve static aeroelastic

problems involving aircraft wings. A loosely coupled approach was preferred as an iterative approach to solve the coupled field problem [38]. Susuz performed static aeroelastic analysis of a typical Unmanned Aerial Vehicle using FlightLoads module of MSC Nastran [39]. Bařkut implemented closely coupled approach to solve static and dynamic aeroelastic problems. Coupling procedure consisted of a commercial flow solver, FLUENT, a finite element solver MSC Nastran and the interference between two solvers was developed [40].

Dababneh performed an optimization analysis in his thesis for the preliminary design phase using MSC Nastran as a structural solver and ESDUpac A9510 as an aerodynamic solver [41]. Ünlüsoy intended to provide the effects of morphing on the linear aeroelastic behavior of unmanned aerial vehicle wings. MSC Nastran was used for finite element modeling of the wings. A steady aerodynamic model was developed by using the experimental pressure data given in NACA report No.563 in order to implement static linear elastic analysis. The unsteady Theodorsen aerodynamics was used in the flutter prediction of the morphing wings [42]. Ünay provided a comprehensive overview of the load analysis process to develop methods for simplifying aircraft structural and aerodynamic models to enable rapid and integrated load analysis in conceptual and preliminary design stages. The structural model was constituted from sectional stiffness values, which were mainly bending and torsional stiffness. The aerodynamic model was simplified using an analytical formulation based on a modified version of the Schrenk Method [43]. Özkaya presented the nonlinear static aeroelastic behavior of composite missile fins induced by interlaminar and intralaminar damage. For this purpose, 3-D finite element models of composite missile wings in different positions were prepared. In this thesis, ANSYS CFX was used for the fluid model (CFD) and ANSYS Mechanical was used for the structural model (FEM) [44].

1.5. Motivation of Thesis

This thesis is mainly focused on the preliminary design phase with the implementation of simple models and it contributes an efficient and practical perspective to the linear and nonlinear static aeroelastic solution methodologies. The simplicity of the models originates from modeling strategy that will be explained in detail in the methodology chapter. Wing planform and section parameters are the only input parameters. Without three-dimensional wing model or finite element model of the wing, aeroelastic behavior at the trim condition can be predicted and divergence speed can be obtained. In the later stages of the design, input parameters can be found by means of sectional analysis tools which determine the cross-sectional properties of the wings. Therefore, the method used in this thesis addresses every stage of design (conceptual, preliminary, and detailed design phases), unlike other methods in the literature.

1.6. Research Objectives

The aim of this thesis is to examine the static aeroelasticity analysis of high aspect ratio wings utilizing different fidelity structural models for the preliminary design stage of the aircraft. Structural models are based on linear and nonlinear theories. The linear structural model is the bending-torsion beam model. The nonlinear structural model is based on the nonlinear torsion finite element method. Aerodynamic models are lifting line theory and lifting surface theory. Coupled aeroelastic models are outlined in Table 1.1. Validation studies are established to confirm the accuracy of structural and aeroelastic methodologies. For the verification, MSC FlightLoads module of MSC NASTRAN® is used which includes the shell model of the wing coupled with Doublet Lattice method (potential theory). Surface spline is preferred as the coupling method.

This research takes a new look at the nonlinear modeling for divergence analysis of the wings by identifying the torsional degree of freedom in the equations of stress-strain relation including the second order term.

Table 1.1. *Outline of the Aeroelastic Models*

Aeroelastic Model	Structural Model	Aerodynamic Model	Applicable for
Model 1	Bending-Torsion Beam Element	Lifting Line Theory	High A/R
Model 2	Bending-Torsion Beam Element	Lifting Surface Theory	Low A/R
Model 3	Nonlinear Torsion Beam Finite Element	Lifting Line Theory	High A/R
Model 4	Nonlinear Torsion Beam Finite Element	Lifting Surface Theory	Low A/R
MSC NASTRAN SOL144	Shell Model	Potential Theory	

1.7. Outline of Thesis

This thesis consists of six main chapters. The first chapter gives a brief overview of the static aeroelasticity and the divergence phenomena. Moreover, it states the scope and delimitations of the thesis. The background information on computational aeroelasticity is presented by mainly focusing on high aspect-ratio wings. Besides, static aeroelasticity studies in the literature are evaluated in a chronological and thematical approach. Finally, the research objectives are given.

In Chapter 2, aerodynamic models used in this thesis are described.

In the third chapter, linear and nonlinear structural models are presented with the derivation of the mathematical theory.

Chapter four outlines the methodologies of the aeroelastic models. For each model iterative process is explained by flowcharts. Attention is drawn to the differences between the models.

Chapter 5 discusses the results of the aeroelastic methods. Structural and aeroelastic models are verified, compared and discussed.

The conclusions together with the possible future work recommendations are outlined in Chapter 6.

CHAPTER 2

AERODYNAMIC MODELS

2.1. Strip Theory (Lifting Line Theory)

2.1.1. Continuous Wing

Strip theory uses the known results of an infinite span airfoil to compute the aerodynamic loading on the wing. Each spanwise location is assumed to be a portion of infinite span wing with uniform cross-section. Hence, it is assumed that the chordwise pressure distribution is based on the local angle of incidence at that spanwise location only and it is not affected by the downwash created by any other location [2].

In strip theory, the wing is assumed to be composed of chordwise strips. For simplicity, lift contributions due to compressibility are ignored at the root and tip locations. Strip theory is applicable for subsonic flow conditions and high aspect ratio wing configurations. It should be noted that drag calculations cannot be performed by the strip theory [45].

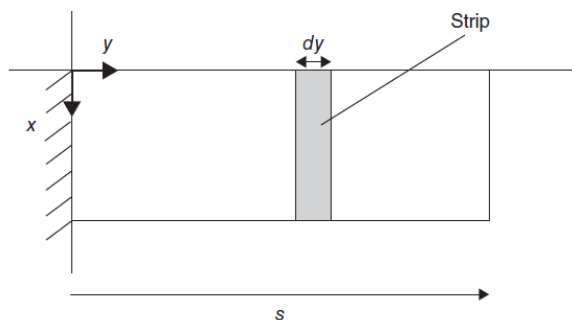


Figure 2.1. Aerodynamic strip on a continuous wing [45]

For a strip element of continuous wing at distance y from the root Figure 2.1, the lift of the increment is described as in Eqn. (2-1).

$$dL = \frac{1}{2} \rho V^2 c dy a_1 \alpha(y) \quad (2-1)$$

where dy is the width of the element and c represents the chord of the wing.

Supposing the lift distribution of a 3D wing is elliptical, in other words, zero lift at tip location, effective lift curve slope can be obtained as in Eqn. (2-2).

$$a_w = \frac{a_1}{1 + a_1 / (\pi AR)} \quad (2-2)$$

The maximum level of reduction in the lift distribution comprises for low aspect ratio wings. Aspect ratio calculation of the wing is given in Eqn. (2-3) [46].

$$AR = \frac{2b}{c} = \frac{(2b)^2}{Area} \quad (2-3)$$

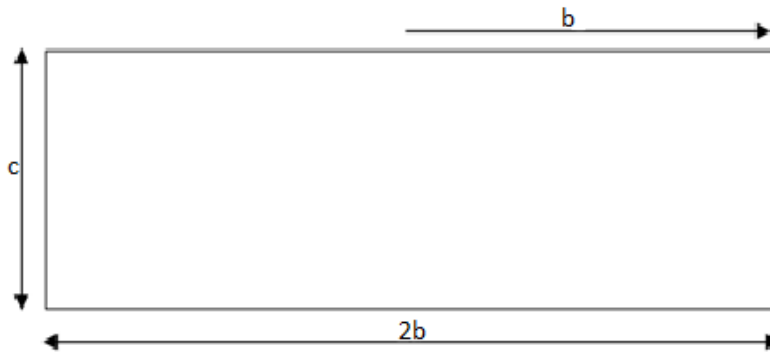


Figure 2.2. Dimensions of a rectangular wing [45]

For tapered wings, the lift estimated by the strip theory reduces across the wing due to the decrease in chord. The effective lift curve slope can be used as a_1 and the strip theory can be modified for the lift reduction across the span by defining the lift curve slope denoted by Eqn. (2-4) to substitute for a_1 .

$$a_w(y) = a_1 \left[1 - \left(\frac{y}{b} \right)^2 \right] \text{ or } a_w(y) = a_1 \left[1 - \left(\frac{y}{b} \right) \right]^2 \text{ or} \quad (2-4)$$

$$a_w(y) = a_1 \cos \left(\frac{\pi y}{2b} \right)$$

2.1.2. Discretized Wing

When the strip theory is to be implemented in conjunction with a finite element method, the formulations represented for the continuous wing can be adapted to the wing sections by considering elemental strips. Delta lift expression can be described in Eqn. (2-5).

$$\Delta L_k = \frac{1}{2} \rho V^2 c \Delta y a_w \alpha(y_k) \quad (2-5)$$

For the tapered wing, the lift expression can be updated in a same way shown for the continuous wing in Eqn. (2-1). The total lift is acquired by the summation of the delta lifts of individual strips given in Eqn. (2-6).

$$L_{Total} = \sum_{k=1}^N \Delta L_k \quad (2-6)$$

The lift curve slope can be adapted for the variational size of the section width Δy .

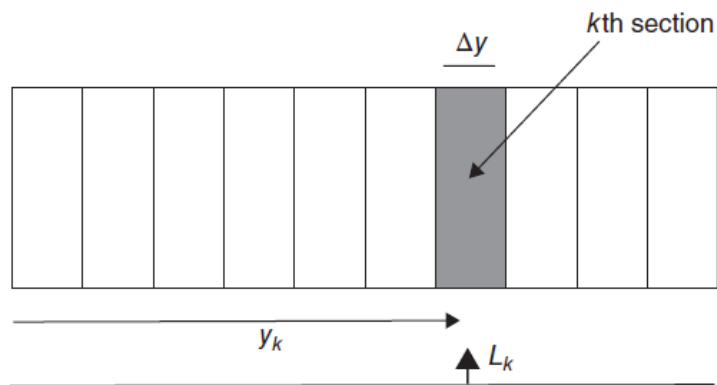


Figure 2.3. Aerodynamic Strips on a discretized rectangular wing [45]

2.2. ESDUpac A9510

ESDUpac A9510 is a computer program based on lifting-surface theory and used to evaluate spanwise lift and moment distributions for low A/R wings in subsonic attached flow. The lifting-surface theory is based on the Multhopp-Richardson's solution [47] [48]. Item No. 83040 is based on ESDUpac A9510 and provides correlation studies for Multhopp-Richardson's solution.

The tool ESDUpac A9510 computes spanwise loading distributions of local lift and pitching moment as a function of incidence angle according to camber and twist data at zero incidence. The loadings can be calculated individually or simultaneously. The inputs for the code are the number of spanwise and chordwise stations for the load calculation, Mach number, loading condition (due to incidence, camber and/or twist) and aspect ratio. The outputs of the code are the spanwise lift and moment distributions and the lift curve slope.

2.2.1. Multhopp-Richardson's Solution

Solution is based on calculation of the local lift and pitching moment at a number of chordwise sections satisfying the downwash conditions at two pivotal points in each section. Interpolation functions are in the trigonometrical form used for getting the resultant forces on the wing from the local forces [48].

With the method of approach to the lifting-surface problem, interpolation polynomials are used, no discontinuity across the middle line can occur. Thus, for the greater part of the median section the physical reality is met better than with an artificial vortex system. The integral equation of the lifting surface is satisfied for only at a limited number of pivotal stations and the interpolation polynomials is satisfied only for the geometrical wing characteristics at these sections. The downwash of an 'interpolated wing' is calculated at which coincides with the real one only in the pivotal sections. All the characteristics of this interpolated wing are accordingly continuous functions of the spanwise.

This downwash integral is dealt with in two stages: firstly, the chordwise integration which leads to elliptical integrals is done numerically for the whole range of relevant positions, assuming the most important chordwise load distributions. The spanwise integration of the downwash is accomplished by a method of approximate integration similar to lifting-line method. Near boundary locations, the integral equation are exactly implemented.

The results of linear system equations are the lifts and the moments per unit span at certain spanwise stations. The solution of this system of equations is performed by iteration, therefore, even for high numbers of pivotal stations can be implemented. The computing effort is adequate and compared to other methods it acquires at a similar precision level.

2.3. Doublet-Lattice Method

The Doublet-Lattice method (DLM) is applicable for any shape of lifting surfaces in subsonic flow. DLM relies on the linearized aerodynamic potential theory. The uniform flow is either steady or varying harmonically. The lifting surfaces are supposed to lie nearly parallel to the flow. DLM is an improved unsteady version of the steady Vortex-Lattice method. DLM is an aerodynamic solver of MSC Nastran.

In DLM, the lifting surfaces are represented as small trapezoidal boxes that are aligned with the free stream velocity. The aerodynamic pressures are assumed to be concentrated at the quarter chord of each boxes. There is one control point per box, centered spanwise on the three-quarter chord line of the box, and the surface normal wash boundary condition is satisfied at each of these points.

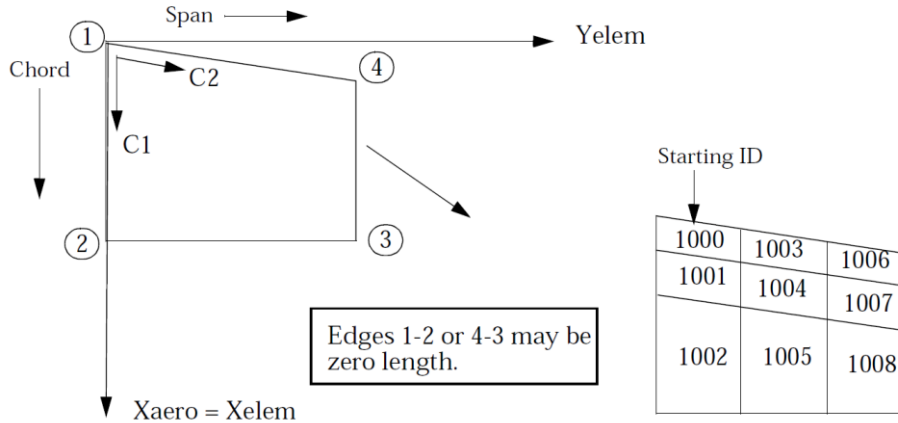


Figure 2.4. Doublet-Lattice Panel Subdivided into Boxes [49]

The aspect ratio of the boxes should be less than three is acceptable in the subsonic case. Boxes should be concentrated near wing edges where downwash is discontinuous, and pressures have large gradients. There is an aerodynamic grid point with its associated degrees of freedom in plunge and pitch for each box within a given panel. These points are located at the center of each box.

The code for computing the aerodynamic influence coefficients A_{jj} was taken from Giesing, Kalman, and Rodden. Aerodynamic symmetry options are available for motions which are symmetric or antisymmetric with respect to one or two orthogonal planes. The full aircraft can also be modeled when the aircraft or its prescribed maneuvers lack symmetry.

The basic relationships between the lifting pressure and the dimensionless vertical or normal velocity induced by the inclination of the surface to the airstream can be formulated as,

$$\{w_j\} = [A_{jj}]\{f_j/q\} \quad (2-7)$$

the differentiation matrix of the deflections to obtain downwash,

$$\{w_j\} = [D_{jk}]\{u_k\} + [D_{jx}]\{u_x\} + \{w_j^g\} \quad (2-8)$$

the integration of the pressure to obtain forces and moments,

$$\{P_k\} = [S_{kj}]\{f_j\} \quad (2-9)$$

where,

w_j	=	downwash
w_j^g	=	static aerodynamic downwash: it includes the static incidence distribution that may arise from an initial angle of attack, camber, or twist
f_j	=	pressure on lifting element j
q	=	flight dynamic pressure
$A_{jj}(m)$	=	aerodynamic influence coefficient matrix, a function of Mach number (m)
u_k	=	displacements at aerodynamic grid points
P_k	=	forces at aerodynamic grid points
D_{jk}	=	differentiation matrix for aerodynamic grid deflection
D_{jx}	=	derivative matrix for the extra aerodynamic points
u_x	=	vector of “extra aerodynamic points” used to describe aerodynamic control surface deflections and overall rigid body motions
S_{kj}	=	integration matrix

Aerodynamic influence matrix can be calculated from the combinations of Eqns. (2-7), (2-8) and (2-9). Final form is given by Eqn. (2-10) which relates the force at an aerodynamic grid to the deflection at that grid.

$$[Q_{kk}] = [S_{kj}][A_{jj}]^{-1}[D_{jk}] \quad (2-10)$$

The interpolation from the structural to aerodynamic degrees of freedom is based upon the theory of splines. High aspect ratio wings, bodies, or other beam-like structures should use linear splines. Low aspect ratio wings, where the structural grid points are distributed over an area, should use surface splines. Several splines can be used to interpolate to the boxes on a panel or elements on a body; however, each aerodynamic box or element can be referenced by only one spline. For all types of splines, the user must specify the structural degrees of freedom and the aerodynamic points involved [49] [50].

CHAPTER 3

STRUCTURAL MODELS

3.1. Linear Structural Models

This section focuses mainly on the linear modeling, which means that material properties remain unchanged with the loading. In mechanical problems, linearity also requires the deformations to be small enough to be written using the undeformed geometry instead of deformed one. In addition, the boundary conditions are assumed not to change during the application of the loads [51].

3.1.1. Bending-Torsion Beam Finite Element Model

A classical approach for developing a mathematical model for the aircraft with high aspect ratio wing is using beam-like models. Beam-like models can be modeled as mathematical models divided by a mesh of finite elements. Finite element (FE) method is a method for the numerical solution of field problems. The displacements and rotations are the unknowns of the analysis. The deformation in each element is estimated approximately using polynomial representations.

The FE approach requires determination of the behavior of the structure in the form of element stiffness matrices and then to assemble all of the element stiffness matrices to generate the global stiffness matrix. The element stiffness matrix assembly process ensures the compatibility of the displacement and rotation between the elements.

Element stiffness matrices are derived from the principle of the potential energy conservation. A displacement form is assumed for the variation within the element. This is partially similar to the Rayleigh-Ritz approach; however, the displacement variation in the whole structure is represented by the sum of the deformed shapes. The Finite Element Methodology is a piecewise form of the Rayleigh-Ritz approach. The

advantages of the Finite Element method are that more elements can be used in the regions where the displacement is expected to change more rapidly and complex geometries with variable cross-sections can be addressed.

3.1.1.1. The Euler-Bernoulli Beam Theory

The Euler-Bernoulli beam theory defines beam element with two-nodes and each node has two degrees of freedom; vertical deflection and rotation. For simplicity, flatwise bending is considered only, assuming that shear, axial or torsion deformation can be ignored.

The nodal displacements denoted by the vector $d = \{d_1 \ d_2 \ d_3 \ d_4\}^T$ are shown in Figure 3.1.

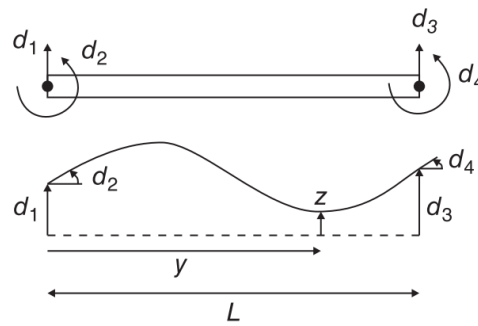


Figure 3.1. Two-node beam bending element

In order to write energy equation terms for the beam element, the variation of the displacement within the element should be expressed in terms of nodal displacements. The variation of transverse displacement z is defined as a cubic polynomial in y ,

$$z = a_0 + a_1y + a_2y^2 + a_3y^3 \quad (3-1)$$

Equation (3-1) is applicable for both of the nodal displacements at the ends of the beam to find the unknown coefficients a_0, \dots, a_3 . The final polynomial after the application of boundary conditions is obtained as,

$$z = N_1d_1 + N_2d_2 + N_3d_3 + N_4d_4 = N^T d \quad (3-2)$$

where N is a vector of shape functions that are shown in Figure 3.2 and they are defined as cubic polynomials in y . For a cantilevered beam, element shape function components are given in Eqns. (3-3) and (3-4) [52].

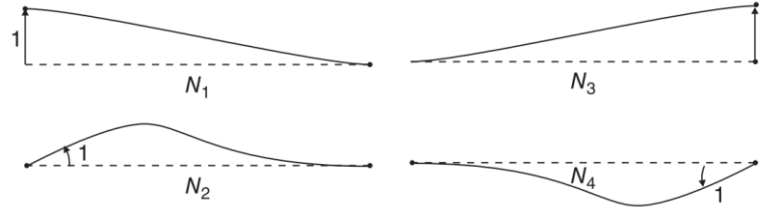


Figure 3.2. Shape functions for a two-node beam element

$$N_1 = 1 - \frac{3y^2}{L^2} + \frac{2y^3}{L^3} \quad N_2 = x - \frac{2y^2}{L} + \frac{y^3}{L^2} \quad (3-3)$$

$$N_3 = \frac{3y^2}{L^2} - \frac{2y^3}{L^3} \quad N_4 = -\frac{y^2}{L} + \frac{y^3}{L^2} \quad (3-4)$$

In the finite element method, forces and moments could be applied at the nodes of the elements as shown in Figure 3.3, these are stated as nodal forces $P = \{P_1 \ P_2 \ P_3 \ P_4\}^T$.



Figure 3.3. Nodal forces for a two-node beam element

The elastic potential energy in bending is based on the curvature and the flexural rigidity. The elastic potential energy equation shown in Eqn. (3-5) is obtained by inserting the elastic curve description into the strain energy in flatwise bending [53].

$$U = \frac{1}{2} \int_0^L EI \left(\frac{\partial^2 z}{\partial y^2} \right)^2 dy \quad (3-5)$$

With the revised displacement description in Eqn. (3-2), the potential energy equation becomes,

$$\begin{aligned}
U &= \frac{1}{2} \int_0^L EI \left(\frac{\partial^2 (N^T d)}{\partial y^2} \right) dy = \frac{1}{2} \int_0^L EI (d^T N'') (N''^T d) dy \\
&= \frac{1}{2} d^T \left[\int_0^L EI (N'' N''^T) dy \right] d
\end{aligned} \tag{3-6}$$

Regarding the similarity between the equation of elastic potential energy in flatwise bending and the strain energy of the rod, $U = \frac{1}{2} kx^2$, the element stiffness matrix can be extracted as in Eqn. (3-7).

$$k = \left[\int_0^L EI (N'' N''^T) dy \right] \tag{3-7}$$

The relevant shape functions are introduced into the stiffness matrix defined in Eqn. (3-7) and matrix multiplications and integrations are performed. For a uniform beam element, final form of the stiffness matrix is obtained as in Eqn. (3-8).

$$k = \frac{EI}{L^3} \begin{bmatrix} 12 & 6L & -12 & 6L \\ 6L & 4L^2 & -6L & 2L^2 \\ -12 & -6L & 12 & -6L \\ 6L & 2L^2 & -6L & 4L^2 \end{bmatrix} \tag{3-8}$$

Consistent load vector is given in Eqn. (3-9). The applied distributed forces, $\{q\}$, should be represented by nodal forces, defined on the basis of equivalent work to the actual distributed forces when the element deforms. In consistent load vector calculations, the same shape functions, N , are used as in the determination of element stiffness matrix. L is the length of element in Eqn. (3-9).

$$\{r_e\} = \int_0^L N^T \{q\} dy \tag{3-9}$$

3.1.1.2. Torsion Bar

Typical two-node torsion bar element is shown in Figure 3.4. The twist for a two-node torsion bar element changes linearly across its length. Hence, shape function is derived as in Eqn. (3-10).

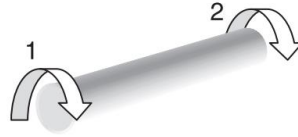


Figure 3.4. Two-node torsion element

$$[N] = \begin{bmatrix} \frac{L-y}{L} & \frac{y}{L} \\ -\frac{y}{L} & \frac{L-y}{L} \end{bmatrix} \quad (3-10)$$

As in Euler-Bernoulli beam element section, the element stiffness matrix can be evaluated based on the elastic potential energy for a member under torsion. The element stiffness matrix is shown in Eqn. (3-11).

$$k = \frac{GJ}{L} \begin{bmatrix} 1 & -1 \\ -1 & 1 \end{bmatrix} \quad (3-11)$$

The consistent load vector is calculated by using shape function given in Eqn. (3-10) according to Eqn. (3-9).

3.1.1.3. Combined Model

Bending-torsion beam structural model is composed of the combination of the Euler-Bernoulli bending beam and the torsion bar. The wing model is represented by the beam model placed at the shear center, as shown in Figure 3.5. There is no bending/torsion stiffness coupling in the stiffness matrix if the mass and elastic axes are coincident.

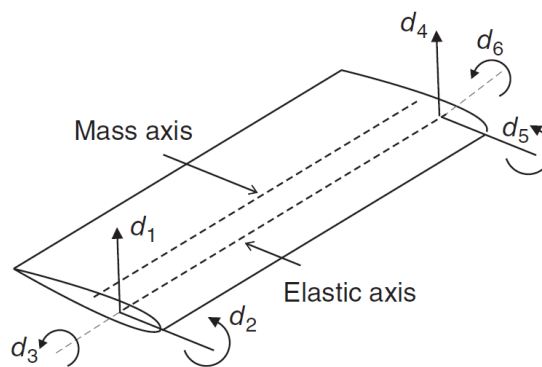


Figure 3.5. Combined bending-torsion beam element [45]

In Figure 3.6, bending-torsion element is shown. The beam is modeled with three degrees of freedom at each node, a vertical deflection w , bending rotation ϕ and twist θ are shown, with corresponding normal force F , moment M and torque T .

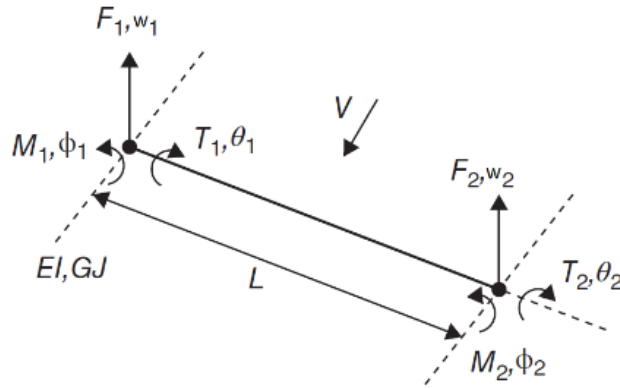


Figure 3.6. Two node beam element

The individually generated stiffness matrices for the bending beam and the torsion bar are expanded to six degrees of freedom, and then combined to compose the element stiffness matrix of bending-torsion beam given in Eqn. (3-12).

$$k = \begin{bmatrix} \frac{12EI}{L^3} & \frac{6EI}{L^2} & 0 & -\frac{12EI}{L^3} & \frac{6EI}{L^2} & 0 \\ \frac{6EI}{L^2} & \frac{4EI}{L} & 0 & -\frac{6EI}{L^2} & \frac{2EI}{L} & 0 \\ 0 & 0 & \frac{GJ}{L} & 0 & 0 & -\frac{GJ}{L} \\ -\frac{12EI}{L^3} & -\frac{6EI}{L^2} & 0 & \frac{12EI}{L^3} & -\frac{6EI}{L^2} & 0 \\ \frac{6EI}{L^2} & \frac{2EI}{L} & 0 & -\frac{6EI}{L^2} & \frac{4EI}{L} & 0 \\ 0 & 0 & -\frac{GJ}{L} & 0 & 0 & \frac{GJ}{L} \end{bmatrix} \quad (3-12)$$

The overall system of the structural equations for combined bending-torsion beam element is shown in Eqn. (3-13) [45].

$$\begin{Bmatrix} F_{w,1} \\ M_{\phi,1} \\ T_{\theta,1} \\ F_{w,2} \\ M_{\phi,2} \\ T_{\theta,2} \end{Bmatrix} = \begin{bmatrix} \frac{12EI}{L^3} & \frac{6EI}{L^2} & 0 & -\frac{12EI}{L^3} & \frac{6EI}{L^2} & 0 \\ \frac{6EI}{L^2} & \frac{4EI}{L} & 0 & -\frac{6EI}{L^2} & \frac{2EI}{L} & 0 \\ 0 & 0 & \frac{GJ}{L} & 0 & 0 & -\frac{GJ}{L} \\ -\frac{12EI}{L^3} & -\frac{6EI}{L^2} & 0 & \frac{12EI}{L^3} & -\frac{6EI}{L^2} & 0 \\ \frac{6EI}{L^2} & \frac{2EI}{L} & 0 & -\frac{6EI}{L^2} & \frac{4EI}{L} & 0 \\ 0 & 0 & -\frac{GJ}{L} & 0 & 0 & \frac{GJ}{L} \end{bmatrix} \begin{Bmatrix} w_1 \\ \phi_1 \\ \theta_1 \\ F_2 \\ \phi_2 \\ \theta_2 \end{Bmatrix} \quad (3-13)$$

Solution procedure involves the computation of the element properties (both stiffness and load), and then, assembling all the elements to form the structure, application of the boundary condition, and finally, solving the assembled Eqn. (3-14) to obtain the nodal displacements.

$$\{R\} = [K_{global}]\{D\} \quad (3-14)$$

For compatibility of the displacements between the assembled elements, the nodal displacements of the mutual nodes of the elements must be equal.

Solution process for the assembled structure can be summarized as follows:

1. The boundary conditions that correspond to zero or prescribed nodal displacements need to be defined
2. The applied loads need to be defined at the unconstraint nodes
3. After the boundary conditions and applied loads are defined, the solution of the structural equations can be obtained by dividing the equation of motion for reactions and for unknown responses.

In Eqn. (3-14), matrix $[K]$ is singular and there is no unique solution for the displacement vector $\{D\}$. Some degrees of freedom in $\{D\}$ must be prescribed in order to have a solution.

By partitioning the structural equations with the rearrangement of the matrix coefficients, may be written as follows [52]:

$$\begin{bmatrix} K_{11} & K_{12} \\ K_{21} & K_{22} \end{bmatrix} \begin{Bmatrix} D_x \\ D_c \end{Bmatrix} = \begin{Bmatrix} R_c \\ R_x \end{Bmatrix} \quad (3-15)$$

where the subscript c symbolizes known quantities, x symbolizes unknown quantities. Therefore, $\{R_c\}$ and $\{D_c\}$ are prescribed loads and degrees of freedom, respectively. The corresponding unknown degrees of freedom for $\{R_c\}$ is $\{D_x\}$, and $\{R_x\}$ stands for the support reactions for the prescribed zero degrees of freedom $\{D_c\}$. If $\{D_c\}$ has sufficient number of degrees of freedom to prevent rigid body motion, $[K_{11}]$ is nonsingular.

Assembling of $[K_{11}]$ matrix is done by the use of ID array. Array ID has as many columns as node numbers and as many rows as degrees of freedom per node. Initially, ID array is null. Then, for each prescribed degrees of freedom, the zero value is replaced with “1”. ID array is converted to a list of equation numbers by changing each 1 to zero. Zeros are not appeared in active degrees of freedom vector, $\{D_x\}$.

Finally, the unknown degrees of freedom can be determined from Eqn. (3-16).

$$\{D_x\} = [K_{11}]^{-1}(\{R_c\} - [K_{12}]\{D_c\}) \quad (3-16)$$

3.2. Nonlinear Torsion Beam Finite Element Model

3.2.1. Overview

The nonlinear problem in structural mechanics concerns with the idea that the stiffness matrix or the load vector is dependent on the displacements.

The linear system can be solved by the use of the linear system equations. On the other hand, nonlinear systems cannot be solved by such simple equations. Actually, nonlinear systems are generally solved by using a sequence of linear analyses.

When the structural system is solved with the linearity assumption, the results may be inaccurate. An example of this is the cantilevered beam under a couple at the tip shown in Figure 3.7. The magnitude of the couple is large enough; hence the beam is subjected to a large deformation.

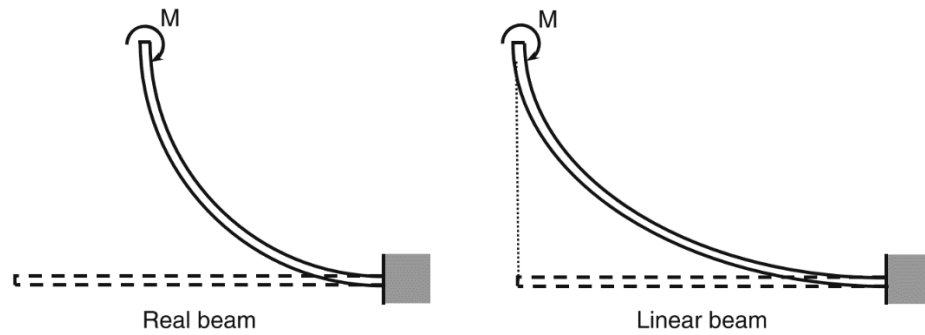


Figure 3.7. Deformation of a beam under a couple

In fact, it is not difficult to imagine that the beam will undergo deformation as shown in the left side of Figure 3.7. In this case, the length of the neutral axis does not change even if the beam undergoes a large deformation. Nevertheless, if a linear theory is used, the beam will be deformed as shown in the right side of Figure 3.7, significantly extending the length of the beam. This is because the linearity assumption ignores the effect of bending moments on the rotation of the neutral axis. Therefore, in linear systems, the length of the beam is always greater than undeformed geometry. When this is the case, the assumption of linearity is clearly not applicable.

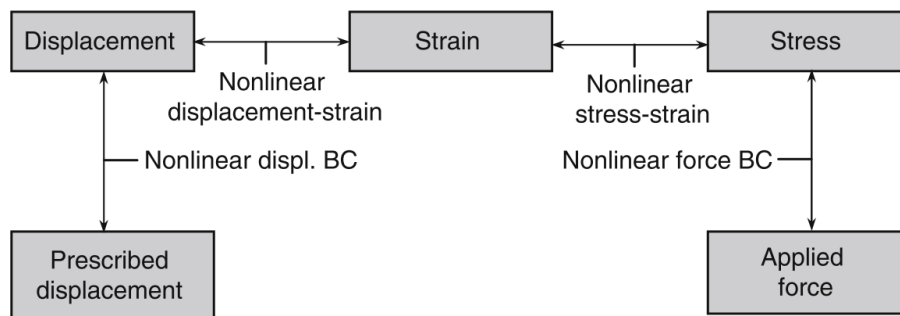


Figure 3.8. Nonlinearities in solid mechanics

Although there are many different approaches to categorize different nonlinearities, it is assumed that four different sources of nonlinearity exist in solid mechanics. Figure 3.8 shows these nonlinearities with their relationship between applied loads, stresses, strains, displacements and boundary conditions [54].

If only the material is nonlinear in an analysis, the nonlinear effects take part only in the nonlinear stress-strain relation. For this type of analysis, the displacements and strains are infinitesimally small, hence engineering stress-strain measures can be utilized in the response definition. Regarding the larger displacement but small strain conditions, infinitesimally small strains measured in a body-attached coordinate frame whereas this frame is exposed to large rigid body displacements and rotations. The stress-strain relation of the material can be either linear or nonlinear. This type of analysis is called as geometrical nonlinearity [51]. If the applied forces are based on the deformation, force nonlinearity arises. According to the deformation of a structure the magnitude and/or direction of the force may change. Frequently, force nonlinearity is accompanied by geometric nonlinearity. The most common example for this type of nonlinearity is the pressure loads of fluids [54]. The analysis of problems in which the boundary conditions change during the motion of the body under consideration. This situation arises in particular in the analysis of contact problems [51]. The most general case contains all types of nonlinearities. However, this type of analysis may end up with a very complex formulation. Also, it may result in high computational cost [54].

In this thesis, the main concern is to find out the effects of geometric nonlinearity on the aeroelastic modeling of high aspect ratio wings. Geometric nonlinearity is accomplished by an incremental and iterative fashion. The solution is searched by partitioning the external loads into load steps which are applied incrementally. After sub-iterating at each load step through a Newton–Raphson technique, the converged configuration has been reached. [33].

3.2.2. Solution Procedure

For the nonlinear equations, it is important to discuss common solution procedures before the finite element formulation. The solution methods applicable to general nonlinear functions are all iterative. The nonlinear equation system is given in Eqn. (3-17),

$$P(u) = f \quad (3-17)$$

where u is a vector of unknowns, f is the applied force, and $P(u)$ is the internal force. In the linear problems, the internal force is a linear function of displacement, i.e. $P(u) = K \cdot u$ with constant stiffness matrix, K . Solving a system of linear equations is equivalent to computing the inverse of K , then multiplying it with applied force vector.

In the nonlinear problems, stiffness matrix depends on the displacements. Solution procedure starts from an initial estimate of displacement, u^0 with the increment Δu . In each iteration cycle, the increment is determined by linearization. After the increment is obtained, the iterative solution process continues until the convergence criterion is met. There are various methods according to the way of calculating the increment.

In order to find the ideal solution method, different iterative procedures should be compared in terms of their advantages and disadvantages. The Newton-Raphson is the most popular method in numerical analysis to detect the roots of the nonlinear equations. If the initial estimate is close to the solution, this method brings about a quadratic convergence. The Newton-Raphson method does not always guarantee a convergence to the right solution. When the determinant of stiffness matrix is zero, solution diverges. Moreover, if the starting point is too far from the accurate solution, the method may diverge.

In each iteration, the Newton-Raphson method requires the creation of the stiffness matrix and the solution of linearized equations. Computational cost is very high. The modified Newton-Raphson method aims to reduce the computational time of this procedure by using the initial stiffness matrix for each of the iteration steps. The usage of fixed stiffness matrix may result in slower convergence.

The objective of the Secant method which is also an iterative method is to presume the stiffness matrix for efficient computation time. In each iteration the Secant method

is faster than the Newton-Raphson method, also it is less expensive, however, the Secant method converges slower than the Newton-Raphson method.

Applying large loads that result in a large displacement causes convergence difficulty. For the incremental force method, load is applied in increments. At each load increment, the iterative solution is based on the standard Newton-Raphson method. The iterative procedure is repeated until the applied load increase reaches its full size. The solution at the end of each load increase is the response of the system corresponding to the given load level.

The Newton–Raphson method is the fastest with a quadratic convergence of all numerical methods, when the initial estimate is close to the solution. In solid mechanics problems, the initial state for the structure is usually chosen as undeformed shape. The Newton -Raphson method converges quickly to the solution if the applied load is small [54]. In this thesis, the Newton-Raphson is chosen as the iterative solution procedure.

In the Newton-Raphson method, the iterative process depends on the approximate solution at the i^{th} iteration specified by u^i . The solution can be approximated by using the first-order Taylor series expansion as shown in Eqn. (3-18).

$$P(u) = f \quad (3-18)$$

$K_T^i(u^i) \equiv (\partial P / \partial u)^i$ is the Jacobian matrix at the i^{th} iteration, widely used as the tangent stiffness matrix and Δu^i is the solution increment. The main purpose is to calculate Δu^i , and then, iteratively update the displacement, u^{i+1} . The linear system of equations is shown in Eqn. (3-19).

$$K_T^i(u^i) \cdot \Delta u^i = f - P(u^i) \quad (3-19)$$

A new approximate solution is estimated as in Eqn. (3-20).

$$u^{i+1} = u^i + \Delta u^i \quad (3-20)$$

This solution does not fulfill the system of nonlinear equations completely. The residual function is obtained as in Eqn. (3-21).

$$R^{i+1} = f - P(u^{i+1}) \quad (3-21)$$

When the residual is smaller than a given tolerance, the result is recognized as the exact solution, and the iteration stops. The termination measure in normalized form is the ‘convergence’ shown in Eqn. (3-22) [54].

$$conv = \frac{\sum_{j=1}^n (R_j^{i+1})^2}{1 + \sum_{j=1}^n (f_j)^2} \quad (3-22)$$

The displacement should be specified first for the force calculation, therefore, it is easy to make the displacement converge instead of the force. The solution-based convergence criterion is shown in Eqn. (3-23) [54].

$$conv = \frac{\sum_{j=1}^n (\Delta u_j^{i+1})^2}{1 + \sum_{j=1}^n (\Delta u_j^0)^2} \quad (3-23)$$

3.2.3. Lagrangian Formulation

In linear systems, it is assumed that there is no significant difference between the deformed and the non-deformed shapes. Hence, the undeformed shape is used to identify the stress and the strain. On the other hand, for large deformations, the difference between the deformed and the non-deformed shapes is large. Therefore, the linear formulations of the stress and the strain equations defined for small deformation assumption should be updated.

When a structure is exposed to some forces and displacements, consequently, its geometry differs from the initial/undeformed to the current/deformed shape as shown in Figure 3.9 [54].

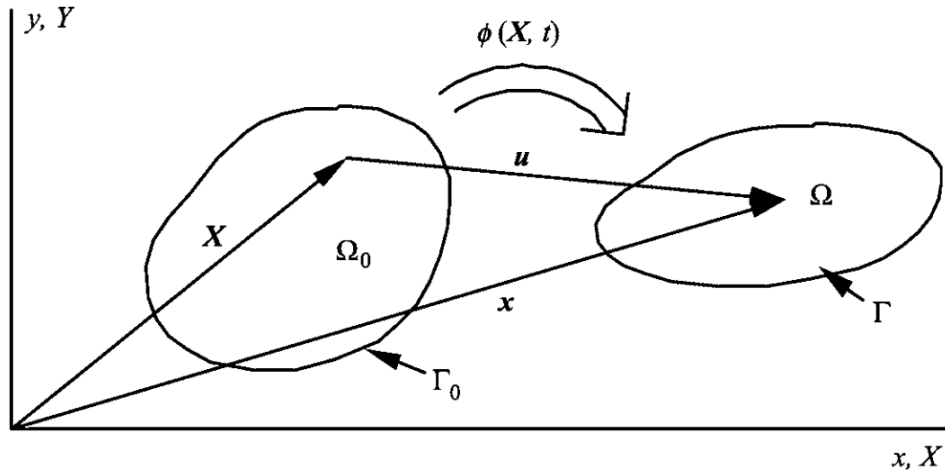


Figure 3.9. Initial/undeformed and the current/deformed states of structure [54]

Unless otherwise specified, the undeformed state is the same as the initial state. The undeformed field is symbolized as Ω_0 in Figure 3.9 and Ω indicates the current configuration. The boundary of the field is demonstrated by Γ which accounts for the end-points of a zone in one dimension.

Two sets of coordinates are used:

- i. Material (Lagrangian) coordinates: $\{X\}$
- ii. Updated Lagrangian (Spatial) coordinates: $x = \{x(X, t)\}$

Lagrangian (material) coordinates utilizes undeformed state as a reference. In Total Lagrangian formulation, stress and strain derivations are obtained according to the material coordinates. Formulations represented by Updated Lagrangian stress and strain derivations are specified according to the spatial coordinates.

Total Lagrangian formulations are employed in the Nonlinear Elastic Nonuniform Torsion structural model.

3.2.4. Derivation of Nonlinear Equations

In this section, the derivation of nonlinear equations is explained in detail before introducing the equations used in the nonlinear theory and the assumption for the

nonlinear structural theory is defined. Equations related to displacements, stress-strain relations and torque-rotation relation are described.

Assumptions

The nonlinear torsion theory is derived considering the following two assumptions for thin walled beams [55].

1. The cross-section is constant, i.e. not deformed in its plane.
2. In the mid-surface, there is no shear deformation.

Displacements

In Figure 3.10, a thin walled I-section beam is demonstrated with its coordinate system.

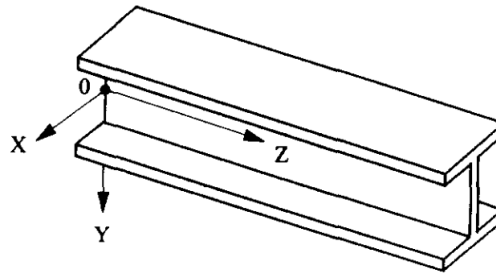


Figure 3.10. Coordinate system of a thin-walled I-beam [55]

For a point P shown in Figure 3.11, based on the assumptions stated above, the displacements in x and y directions due to the arbitrary rotation, Φ of the cross-section around the z axis, can be written as in Eqns. (3-24) and (3-25) .

$$u = x_1 - x = r \cos(\alpha + \Phi) - x = x(\cos\Phi - 1) - y \sin\Phi \quad (3-24)$$

$$v = y_1 - y = r \sin(\alpha + \Phi) - y = y(\cos\Phi - 1) + x \sin\Phi \quad (3-25)$$

In Eqns. (3-24) and (3-25), r is the radial distance from the origin. Equations are valid for large rotation Φ .

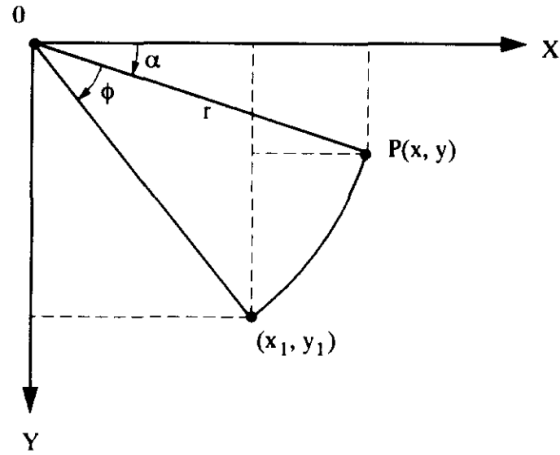


Figure 3.11. Transverse displacements of the cross-section [55]

Warping Displacements

It is assumed that longitudinal warping displacement w in the z direction ($\partial w/\partial z$) is less than unity. Second assumption dictates that the shear strain at the mid-surface of the beams are zero as shown in Eqn. (3-26).

$$\gamma_{xz} = \frac{\partial u}{\partial z} + \frac{\partial w}{\partial x} + \left(\frac{\partial u}{\partial x} \frac{\partial u}{\partial z} + \frac{\partial v}{\partial x} \frac{\partial v}{\partial z} \right) = 0 \quad (3-26)$$

Substituting Eqns. (3-24) and (3-25) into Eqn. (3-26), final form is obtained as Eqn. (3-27).

$$\frac{\partial w}{\partial x} - y\Phi' = 0 \quad (3-27)$$

Similarly, substituting Eqns. (3-24) and (3-25) into Eqn. (3-28), Eqn. (3-29) can be obtained.

$$\gamma_{yz} = \frac{\partial u}{\partial z} + \frac{\partial w}{\partial y} + \left(\frac{\partial u}{\partial y} \frac{\partial u}{\partial z} + \frac{\partial v}{\partial y} \frac{\partial v}{\partial z} \right) = 0 \quad (3-28)$$

$$\frac{\partial w}{\partial y} + x\Phi' = 0 \quad (3-29)$$

Warping displacements in the z direction are supposed to be negligible. Integrating Eqns. (3-27) and (3-29) one ends up with Eqn. (3-31) where ω is the warping function. The equation of the warping function is given by Eqn. (3-30) [56].

$$\omega = \frac{1}{A} \int_A \left\{ \int_0^{s_c} \rho_0 ds_c \right\} t ds_c - \int_0^{s_c} \rho_0 ds_c \quad (3-30)$$

ρ_0 = Perpendicular distance from shear center
 s_c = Distance around mid-thickness line

Due to the small shear strains, warping as a result of shear strain is neglected. It is assumed that warping is due to the twisting alone.

$$w = -\omega \Phi' \quad (3-31)$$

Longitudinal Normal Strains

The nonlinear longitudinal formulation is given in Eqn. (3-32).

$$\varepsilon_z = \frac{\partial w}{\partial z} + \frac{1}{2} \left[\left(\frac{\partial u}{\partial z} \right)^2 + \left(\frac{\partial v}{\partial z} \right)^2 \right] \quad (3-32)$$

By substituting Eqns. (3-24), (3-25) and (3-31) into Eqn. (3-32), final equation is obtained as in Eqn. (3-33).

$$\varepsilon_z = -\omega \Phi'' + \frac{1}{2} (x^2 + y^2) \Phi'^2 \quad (3-33)$$

The term $\frac{1}{2} (x^2 + y^2) \Phi'^2$ is the second-order geometric nonlinear term and it is described as the Wagner effect which gives the coupling of the torsional and axial deformation.

Shear Strains

The shear strain distribution due to uniform torsion is approached by the mitre model of shear distribution which serves a good approximation for elastic torque-twist relationship [57].

$$\gamma_u = \Omega\Phi' \quad (3-34)$$

where

$$\begin{aligned} \gamma_u &= \text{uniform torsion shear strain} \\ \Omega &= \text{uniform torsion shear strain function} \\ \Phi' &= \text{derivative of twist rotation of cross-section about the z axis} \end{aligned}$$

Strain-Rotation Relationships

For the point P, the normal and shear strain formulations given in Eqns. (3-33) and (3-34) can be combined together to form Eqn. (3-35)

$$\{\varepsilon_p\} = \begin{Bmatrix} \varepsilon_w \\ \gamma_u \end{Bmatrix} = [S]\{\varepsilon\} \quad (3-35)$$

where,

$$[S] = \begin{bmatrix} -\omega & (x^2 + y^2) & 0 \\ 0 & 0 & \Omega \end{bmatrix} \quad (3-36)$$

$$\{\varepsilon\} = \begin{Bmatrix} \Phi'' \\ \frac{1}{2}\Phi'^2 \\ \Phi' \end{Bmatrix} \quad (3-37)$$

The strain vector can be resolved into linear and quadratic components as shown in Eqn. (3-38).

$$\{\varepsilon\} = [B_L + B_Q]\{\Phi\} \quad (3-38)$$

where,

$$\{\Phi\} = \{\Phi' \quad \Phi''\}^T \quad (3-39)$$

$$[B_L]^T = \begin{bmatrix} 0 & 0 & -1 \\ -1 & 0 & 0 \end{bmatrix} \quad (3-40)$$

$$[B_Q]^T = \begin{bmatrix} 0 & \Phi'/2 & 0 \\ 0 & 0 & 0 \end{bmatrix} \quad (3-41)$$

Differentiating Eqn. (3-38) with respect to z leads to Eqn. (3-44).

$$\{\delta\varepsilon\} = [B_L]\{\delta\Phi\} + \delta([B_Q] + \{\Phi\}) \quad (3-42)$$

$$[\delta B_Q]\{\Phi\} = [B_Q]\{\delta\Phi\} \quad (3-43)$$

$$\{\delta\varepsilon\} = [B_L + 2B_Q]\{\delta\Phi\} \quad (3-44)$$

The rotational displacements can be evaluated by the element nodal degrees of freedom as shown in Eqn. (3-45). The shape function matrix $[N]$ relates displacement of the shear center to nodal degrees of freedom, $\{\delta\Phi\}$.

$$\{\Phi\} = [N]\{\delta\Phi\} \quad (3-45)$$

where,

$$\{\delta_\Phi\} = \{\Phi_1 \ \Phi_2 \ \Phi_1' \ \Phi_2'\}^T \quad (3-46)$$

Stress-Strain Relationships under Combined Stresses

When the applied load is small, the material is in an elastic state, therefore, the stress-strain relationship is based on Hooke's law of flexibility shown in Eqn. (3-47). After removing the external force, the structure attains completely its initial form [58].

$$\{\sigma_p\} = [D_e]\{\varepsilon_p\} \quad (3-47)$$

where,

$$\{\sigma_p\} = \begin{Bmatrix} \sigma_w \\ \tau_u \end{Bmatrix} \quad (3-48)$$

Generalized elasticity matrix (elastic moduli matrix) is given in Eqn. (3-49).

$$[D_e] = \begin{bmatrix} E & 0 \\ 0 & G \end{bmatrix} \quad (3-49)$$

As the applied load increases, the material may get into the inelastic range, as a result, the linear relationship no longer prevails. On the contrary, the stress-strain behavior is ruled by the elastic-plastic incremental relationship demonstrated in Eqn. (3-50).

$$d\{\sigma_p\} = [D_{ep}]d\{\varepsilon_p\} \quad (3-50)$$

where the elastic-plastic strain matrix derived from the plastic Prandtl-Reuss flow rule,

$$[D_{ep}] = [D_e] - [D_p] \quad (3-51)$$

In this thesis material nonlinearity is out of the topic. In other words, the applied force is assumed to be small enough to handle the material in the elastic region. Therefore $[D_{ep}]$, the derivative form of the generalized elasticity matrix, is treated as $[D_e]$ from now on.

Torque-Rotation Relationships

The equilibrium formulations based on the principle of virtual work is given by Eqn. (3-52) where $\{F\}$ represents the nodal external forces equivalent to internal resistances.

$$\int \delta\{\varepsilon_p\}^T \{\sigma_p\} dv - \{\delta\Phi\}^T \{F\} = 0 \quad (3-52)$$

Substituting Eqns. (3-35), (3-44) and (3-45) into Eqn. (3-52),

$$\int [N]^T [B_L + 2B_Q]^T [S]^T \{\sigma_p\} dv - \{F\} = 0 \quad (3-53)$$

In general, the equilibrium equation cannot be achieved, but it causes a series of errors shown in Eqn. (3-54).

$$\{e\} = \int [N]^T [B_L + 2B_Q]^T [S]^T \{\sigma_p\} dv - \{F\} \quad (3-54)$$

The first-order Taylor series expansion is utilized to achieve an approximate solution. By increasing $\{\delta\Phi\}$ to $\{\delta\Phi + \Delta\delta\Phi\}$ generates Eqn. (3-55).

$$\{e(\{\delta\Phi + \Delta\delta\Phi\})\} \approx \{e(\{\delta\Phi\})\} + [de/d\delta\Phi]\{\Delta\delta\Phi\} \quad (3-55)$$

Consequently, the following formulation is obtained.

$$[K_T]\{\Delta\delta\Phi\} = \{\Delta e\} \quad (3-56)$$

$[K_T]$ is the tangent stiffness matrix given by Eqn. (3-57).

$$[K_T] = [de/d\delta\Phi] \quad (3-57)$$

Inserting Eqn. (3-54) into Eqn. (3-57) results in Eqn. (3-58).

$$[K_T]\{d\delta\Phi\} = \int_V [N]^T \left([B_L + 2B_Q]^T [S]^T d\{\sigma_p\} + 2[dB_Q]^T [S]^T \{\sigma_p\} \right) dv \quad (3-58)$$

Substituting Eqns. (3-35), (3-44), (3-45) and (3-47) into the definition of $d\{\sigma_p\}$, Eqn. (3-59) is obtained.

$$[K_T]\{d\delta\Phi\} = \int_V [N]^T \left([B_L + 2B_Q]^T [S]^T [D_e][S][B_L + 2B_Q][N]\{d\delta\Phi\} + 2[dB_Q]^T [S]^T \{\sigma_p\} \right) dv \quad (3-59)$$

The tangent modulus constitutive matrix $[D]$ is given in Eqn. (3-60).

$$[D] = \int_A [S]^T [D_e][S] dA \quad (3-60)$$

Final form of the matrix is obtained as in Eqn. (3-61).

$$[D] = \begin{bmatrix} EI_W & 0 & 0 \\ 0 & EI_n & 0 \\ 0 & 0 & GJ \end{bmatrix} \quad (3-61)$$

where for narrow cross-section

$$I_W = \int_A \omega^2 dA \quad (3-62)$$

$$I_n = c^5 t / 180 \quad (3-63)$$

$$J = \frac{1}{3} ct^3 \quad (3-64)$$

The generalized stress vector is given by Eqn. (3-65).

$$\{\sigma\} = \int_A [S]^T \{\sigma_p\} dA \quad (3-65)$$

Final form of the generalized stress vector is obtained as in Eqn. (3-66).

$$\{\sigma\}^T = \{-EI_W\Phi'' \quad EI_n(\Phi')^2/2 \quad -GJ\Phi'\} \quad (3-66)$$

Equation (3-67) can be rewritten as,

$$\begin{aligned} [K_T]\{d\delta\Phi\} = \int_L [N]^T \left([B_L + 2B_Q]^T [D][B_L + 2B_Q][N]\{d\delta\Phi\} \right. \\ \left. + 2[dB_Q]^T \{\sigma\} \right) dz \end{aligned} \quad (3-67)$$

By defining the geometric matrix, tangent matrix is derived as in Eqn. (3-68).

$$[K_T] = \int_L [N]^T \left([B_L + 2B_Q]^T [D][B_L + 2B_Q] + [M_\sigma] \right) [N] dz \quad (3-68)$$

where,

$$2[dB_Q]^T \{\sigma\} = [M_\sigma][N]\{d\delta\Phi\} \quad (3-69)$$

Geometric matrix is evaluated by integrating both sides of Eqn. (3-69), and then inserting Eqns. (3-45) and (3-66) in Eqn. (3-69). $[M_\sigma]$ is given by Eqn. (3-70).

$$[M_\sigma] = \begin{bmatrix} EI_n(\Phi')^2/2 & 0 \\ 0 & 0 \end{bmatrix} \quad (3-70)$$

The stiffness matrix, given in Eqn. (3-71) is composed of a small displacement component, a large displacement component and a geometric component, respectively.

$$[K_T] \approx [K_L] + [K_Q] + [K_\sigma] \quad (3-71)$$

$$[K_L] = \int_L [N]^T [B_L]^T [D][B_L][N] dz \quad (3-72)$$

$$[K_Q] = \int_L [N]^T \left([B_L]^T [D][2B_Q] + [2B_Q]^T [D][B_L] \right) [N] dz \quad (3-73)$$

$$[K_\sigma] = \int_L [N]^T [M_\sigma][N] dz \quad (3-74)$$

3.2.5. Nonlinear Elastic Nonuniform Torsion Beam

The previous section explains where the nonlinear formulations come from. In this section, the formulations used in coding are summarized.

The elastic nonuniform torsion of thin-walled beams is usually modeled as linear, but at high angles of twist rotation, longitudinal stresses induced by the axial shortening of the longitudinal fibers cause significant nonlinear stiffening and strengthening effects. The basic differential equation for nonlinear elastic nonuniform torsion is given by Eqn. (3-75) [59].

$$M_z = GJ \frac{d\Phi}{dz} - EI_W \frac{d^3\Phi}{dz^3} + \frac{1}{2} EI_n \left(\frac{d\Phi}{dz} \right)^3 \quad (3-75)$$

where,

$$\begin{aligned} M_z &= \text{Torque at a distance } z \text{ along the torsion member} \\ I_W &= \text{Warping section constant} \\ I_n &= \text{Nonlinear Wagner constant} \end{aligned}$$

A finite element computer program has been developed for the elastic analysis of nonlinear torsion based on the work of Trahair [59]. For this, the member length is divided into a number of elements. The typical element used has a cubic twist rotation field defined in Eqn. (3-76) which has similar form with the linear Eqn. (3-1).

$$\Phi = a_0 + a_1(z/L) + a_2(z^2/L^2) + a_3(z^3/L^3) \quad (3-76)$$

where L is the element length, and z is the distance along the element. Equation (3-76) can be written in a generic form as,

$$\Phi = \{Z\}^T \{a\} \quad (3-77)$$

where,

$$\{Z\}^T = \{1 \ z/L \ (z/L)^2 \ (z/L)^3\} \quad (3-78)$$

and

$$\{a\} = \{a_0 \ a_1 \ a_2 \ a_3\}^T \quad (3-79)$$

The field $\{a\}$ has undetermined constants, a_n that can be changed by the nodal degrees of freedoms. Substituting end values of z and making appropriate differentiations of Eqn. (3-76), Eqn. (3-80) can be obtained.

$$\{\delta_\phi\} = \{\Phi_1 \ \Phi_2 \ \Phi'_1 \ \Phi'_2\}^T \quad (3-80)$$

Here $' \equiv d/dz$, Φ_1 and Φ_2 are values of twist (Φ) at the element ends and Φ'_1 and Φ'_2 are the values of Φ' at the element ends. As a result, the relation between undetermined constants a_n and Φ_n is derived as in Eqn. (3-81).

$$\{\delta_\phi\} = [C_\phi]\{a\} \quad (3-81)$$

where,

$$[C_\phi] = \begin{bmatrix} 1 & 0 & 0 & 0 \\ 1 & 1 & 1 & 1 \\ 0 & 1/L & 0 & 0 \\ 0 & 1/L & 2/L & 3/L \end{bmatrix} \quad (3-82)$$

Equation (3-81) is reversed as shown in Eqn. (3-83).

$$\{a\} = [C_\phi]^{-1}\{\delta_\phi\} \quad (3-83)$$

where,

$$[CI] = [C_\phi]^{-1} = \begin{bmatrix} 1 & 0 & 0 & 0 \\ 0 & 0 & L & 0 \\ -3 & 3 & -2L & -L \\ 2 & -2 & L & L \end{bmatrix} \quad (3-84)$$

Therefore, the deformation equation can be rewritten as given in Eqn. (3-84) replacing $[C_\phi]^{-1}$ with $[CI]$ [60]. Substitute Eqn. (3-84) into Eqn. (3-83) and by using Eqn. (3-77), Eqn. (3-85) can be obtained.

$$\Phi = \{Z\}^T [CI] \{\delta_\phi\} \quad (3-85)$$

The deformation vector is given by Eqn. (3-86).

$$\{\Phi\} = \{\Phi' \quad \Phi''\}^T \quad (3-86)$$

The rotation vector can be found from the nodal deformations vector, $\{\delta_\phi\}$ as shown in Eqn. (3-87).

$$\{\Phi\} = [N_\sigma]\{\delta_\phi\} \quad (3-87)$$

Substitute Eqn. (3-85) into Eqn. (3-86) calculate Φ' and Φ'' , and then substitute them into Eqn. (3-87), the shape function matrix is obtained as in Eqn. (3-88).

$$[N_\sigma] = \begin{bmatrix} \{Z'\}^T \\ \{Z''\}^T \end{bmatrix} [CI] \quad (3-88)$$

In the form of equilibrium relationship, Eqn. (3-89) is written between the external actions and the internal forces.

$$\{F_E\} = \{F_I\} \quad (3-89)$$

In Eqn. (3-89), the external actions are the nodal torques consisting of the applied concentrated torques and the equivalents of the distributed torques per unit length.

Internal forces are given by,

$$\{F_I\} = \int_0^L [N_\sigma]^T [B_L + 2B_Q]^T \{\sigma\} dz \quad (3-90)$$

and the tangent stiffness matrix from Eqn. (3-68) by substituting $[N_\sigma]$ instead of $[N]$ (for twist rotation only),

$$[K_T] = \int_0^L [N_\sigma]^T ([B_L + 2B_Q]^T [D] [B_L + 2B_Q] + [M_\sigma]) [N_\sigma] dz \quad (3-91)$$

In general, the equilibrium Eqn. (3-89) will not be satisfied, and lead to a set of errors,

$$\{e\} = \{F_E\} - \{F_I\} \quad (3-92)$$

which may be reduced by introducing a set of deformation changes $\{\Delta\delta_\phi\}$ which satisfy,

$$[K_T]\{\Delta\delta_\phi\} = \{e\} \quad (3-93)$$

These changes may be performed iteratively until the errors $\{e\}$ are sufficiently small. At each load increment, the equation is solved iteratively by the Newton–Raphson procedure.

Initially, an initial estimate is assumed for twist distribution, Φ , and the increment $\Delta\delta_\phi$ is obtained. New estimate is $\Phi^0 + \Delta\delta_\phi$. In order to find the increment, the nonlinear equations are approximated by linear equations. This process is repeated until the convergence criterion is satisfied [54] [56].

CHAPTER 4

STATIC AEROELASTIC MODELS

The solution methodology is an aeroelastic type of solution combining structural and aerodynamic models. The initial torsional displacement of the wing is assumed zero for all the structural models and the aerodynamic model is solved with this assumption. The obtained aerodynamic loads are fed into the aeroelastic equations to solve for the new torsional deflection which is the next input for the new aerodynamic load calculation. The iterative procedure is continued until the predefined convergence criterion is reached. This loop is repeated for every dynamic pressure.

Analyses are performed with three different structural models coupled with strip theory and lifting surface theory for a simple plate-like wing model.

4.1. Bending-Torsion Beam Finite Element based Aeroelastic Model (Model 1 & Model 2)

Model 1 represents bending torsion beam finite element model coupling with Strip theory (lifting line theory) and Model 2 is composed of bending-torsion finite element model and ESDUpac A9510 (lifting surface theory).

Iterative solution process is outlined in the flowchart presented in Figure 4.1. Iterative solution starts after the initialization of structural and aerodynamic models. In each iterative calculation, aerodynamic forces are generated according to the deformed structure. The interaction between structural and aerodynamic models is accomplished by force and displacement splines which are interpolation functions to transfer information of force and displacement between the structure and aerodynamic models [35].

The iteration is continued until the tolerance criterion is reached. When the torsional deformation is greater than the limiting value of 30 degrees, the process is stopped, and the current dynamic pressure at that stage is the divergence dynamic pressure.

The system of the structural equations for combined bending-torsion beam element is shown in Eqn. (3-13). Consistent external load vectors are calculated for aerodynamic lift and moment and they are applied at the nodes of the element.

Computational procedure can be summarized as constitution of element matrices, then assembling all the element matrices to form the global stiffness and load matrices, application of the boundary condition and finally solving the assembled Eqn. (3-14) to obtain the displacements.

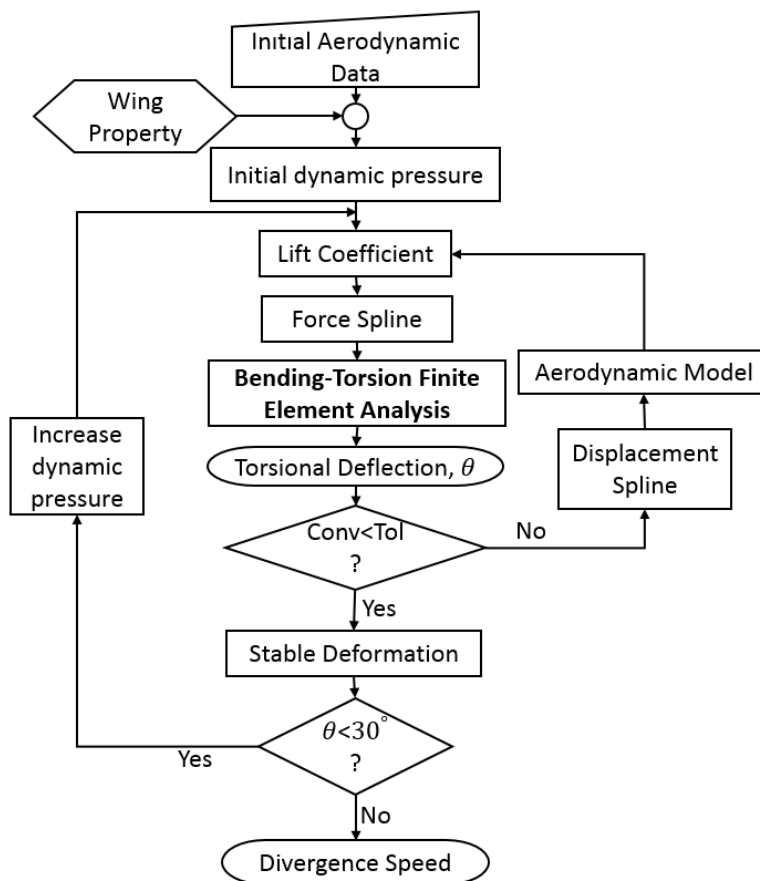


Figure 4.1. Iterative process of Model 1 & Model 2

4.2. Nonlinear Torsion Beam Finite Element based Aeroelastic Model (Model 3 & Model 4)

Model 3 and Model 4 are composed of nonlinear torsion beam finite element model coupling with Strip theory (lifting line theory) and ESDUpac A9510 (lifting surface theory), respectively.

This calculation requires rotation of the aerodynamic force matrices which are initially generated in the non-deformed state of each iteration of the Newton-Raphson procedure based on the previous convergent deformed configuration. The iterative process is shown in Figure 4.2.

Basically, once the nonlinear procedure converges, then the aeroelastic iteration starts. The convergence criteria is shown in Eqn. (3-23). When the convergence criteria of the aeroelastic loop is provided, stable deformation is obtained at the current dynamic pressure. Then for the new external load, $\{F_E\}$, nonlinear procedure is implemented and so on. The analysis stops when the torsional deflection is greater than 30 degrees.

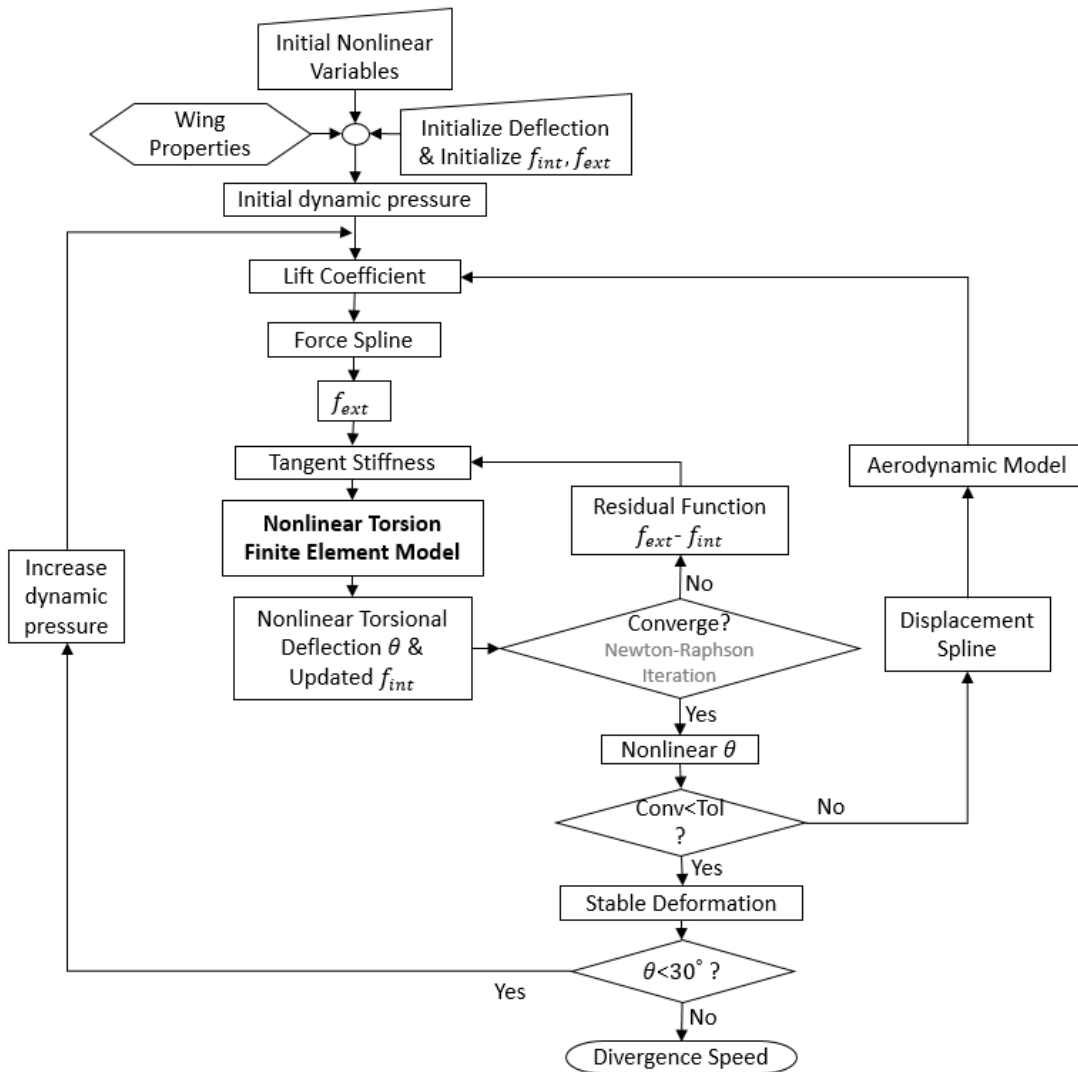


Figure 4.2. Iterative process of Model 3 and Model 4

4.3. NASTRAN Verification Model with SOL144

This model is composed of the coupling of Doublet-Lattice model (DLM) and shell model of the wing. Aerodynamic and structural models are connected to each other by surface spline. For the spline creation, entire aerodynamic surface must be included and the selection of load carrying member from the structural model is sufficient. After the coupling of aerodynamic surfaces and structural model is completed, modal analysis is performed.

Divergence analysis is implemented by the trim method and as a result, divergence dynamic pressure is obtained. In MSC Nastran divergence analysis is executed based on Eqn. (4-1), complete equations of motions in the a-set degrees of freedom.

$$[K_{aa} - \bar{q}Q_{aa}]\{u_a\} + [M_{aa}]\{\ddot{u}_a\} = \{P_a\} \quad (4-1)$$

\bar{q} = flight dynamic pressure
 u_a = structural deflections

Aerodynamic influence coefficient matrix represented as Q_{aa} provides the forces at the structural grid points due to structural deformations. Q_{ax} provides forces at the structural grid points due to unit deflections of the aerodynamic points. K_{aa} is the structural stiffness matrix and M_{aa} is the structural mass matrix. P_a is vector of applied loads, for the thesis external force is aerodynamic load.

Eqn. (4-1) is partitioned into r-set (supported) and l-set (left over) degrees of freedom yielding,

$$\begin{bmatrix} K_{ll}^a & K_{lr}^a \\ K_{rl}^a & K_{rr}^a \end{bmatrix} \begin{Bmatrix} u_l \\ u_r \end{Bmatrix} + \begin{bmatrix} M_{ll} & M_{lr} \\ M_{rl} & M_{rr} \end{bmatrix} \begin{Bmatrix} \ddot{u}_l \\ \ddot{u}_r \end{Bmatrix} = \begin{Bmatrix} P_l \\ P_r \end{Bmatrix} \quad (4-2)$$

where,

$$[K_{aa}^a] = [K_{aa} - \bar{q}Q_{aa}] \quad (4-3)$$

The divergence speeds of a restrained aircraft component may be obtained by solving an eigenvalue problem. The divergence eigenvalue problem for the restrained vehicle can be extracted from the (1,1) partition of Eqn. (4-2).

$$[K_{ll}^a]\{u_l\} = 0 \quad (4-4)$$

Since from Eqn. (4-3), $[K_{ll}^a] = [K_{ll} - \bar{q}Q_{ll}]$; therefore, divergence eigenvalue problem becomes

$$[K_{ll} - \lambda Q_{ll}]\{u_l\} = 0 \quad (4-5)$$

u_l = deflection of the support points (fixed)

The eigenvalues (λ) are the dynamic pressures for divergence, \bar{q}_D . Only positive values of \bar{q}_D have physical significance and the lowest value of \bar{q}_D is the critical divergence dynamic pressure [50] [49].

Divergence solution procedure of SOL144 is shown in Figure 4.3.

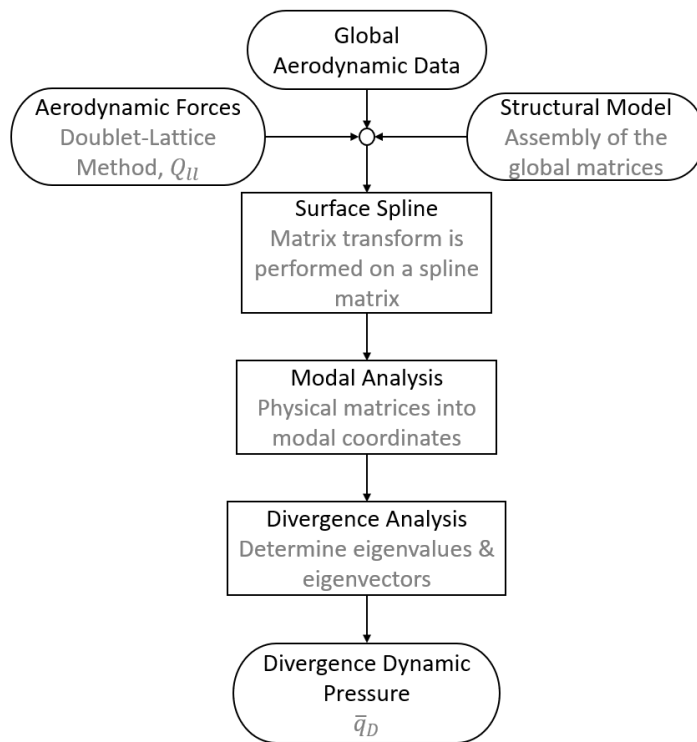


Figure 4.3. Flowchart of SOL144

CHAPTER 5

RESULTS

5.1. Patil-Hodges Wing

The wing model considered in this thesis is based on the work of Patil and Hodges and illustrated in Figure 5.1 [24] [25] [61]. The un-swept, high aspect ratio wing is modeled as a simple plate-like wing for aeroelastic analysis. The wing indicates sufficient flexibility to take the geometric nonlinearity into consideration. NACA0012 is selected as the wing cross-section profile. Design parameters and the flight conditions of the wing model is given in Table 5.1 and Table 5.2, respectively.

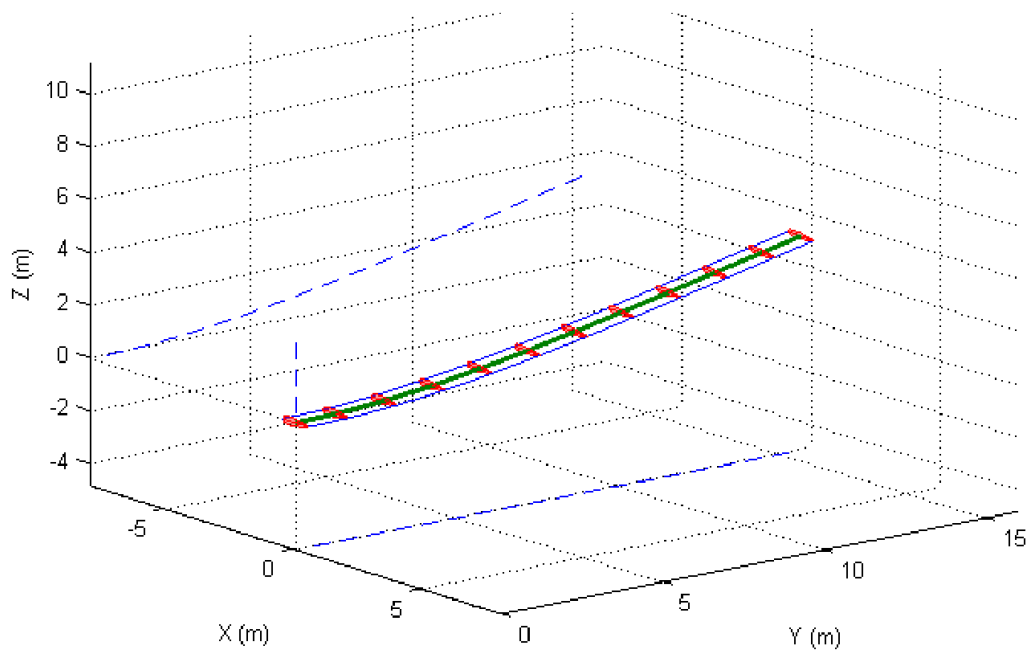


Figure 5.1. Patil-Hodges wing [32]

Table 5.1. Design Parameters of Patil-Hodges Wing [24] [25] [61]

Symbol	Value	Unit	Description
b	16	m	Half span of the wing
c	1	m	Chord of the wing
m/b	0.75	kg/m	Mass per unit length
AR	32	-	Aspect ratio of the wing
c_t/c_r	1	-	Taper ratio of the wing
ea.	%50 chord	-	Spanwise elastic axis
cg.	%50 chord	-	Centre of gravity
ac.	%25 chord	-	Aerodynamic center
EI_{xx}	2×10^4	Nm^2	In-Plane Bending rigidity
EI_{zz}	2×10^4	Nm^2	Out-of-Plane Bending rigidity
GJ	0.636×10^4	Nm^2	Torsional rigidity
I_w	0	m^6	Wagner section constant

Table 5.2. Flight Conditions of Patil-Hodges Wing [24] [25] [61]

Parameter	Value	Unit
Altitude	20	km
Density of air	0.0889	kg/m^3

The Patil-Hodges wing is modeled using shell elements (PSHELL) in MSC Nastran. Figure 5.2 shows the MSC Nastran finite element representation of the structural model based on the properties shown in Table 5.1. Shell model of the Patil-Hodges wing is verified according to linear static and normal modes analyses results given in the literature [24] [29] [33].

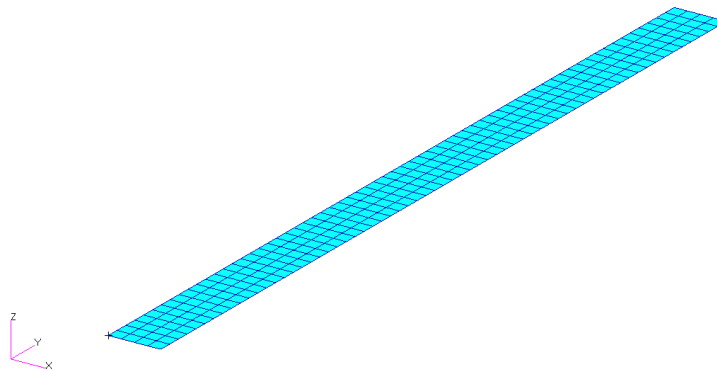


Figure 5.2. Structural Model of Patil-Hodges Wing

By using the known values of EI_{xx} and EI_{zz} from Table 5.1, the thickness of the simple plate is calculated as 0.0707m.

$$I_{xx} = \frac{1}{12} ct^3 \quad (5-1)$$

$$I_{zz} = \frac{1}{12} tc^3 \quad (5-2)$$

According to calculated thickness and known chord values, G is calculated from the GJ value given in Table 5.1 using Eqn. (5-3).

$$J = \frac{1}{3} ct^3 \quad (5-3)$$

As a matter of fact, 3D model of the Patil-Hodges wing has ribs, for an accurate simplification simple plate is modeled as orthotropic instead of isotropic material because actual wing model does not show the same characteristics in all directions.

Since the wing model shared in the literature does not cover the properties of orthotropic material, sensitivity analyzes are performed to provide the results of the given modal analysis results in the literature [33] and the converged material properties are given in Table 5.3.

Table 5.3. *Shell model orthotropic material properties*

Symbol	Value	Unit	Description
$E_{11} = E_{22}$	6.79E8	Pa	Young's moduli in the longitudinal, lateral directions, respectively
G_{12}	5.40E7	Pa	In-plane shear modulus
$G_{13} = G_{23}$	5.40E7	Pa	Transverse shear modulus for shear in the 1-3 and 2-3 plane, respectively
ρ	10.607	kg/m^3	Density

Table 5.4 represents modal behavior of the shell model. Table 5.4 was made to determine the appropriate number of elements to be included in the model in order to give a reasonable accuracy to the overall solution. The model with 160x10 grids is chosen for the further investigations by considering accuracy of the results.

Table 5.4. Comparison of linear frequency results (Hz) of shell model with the test case [24]

Mode ID	Mode Description	Shell Model Grid: 64x4	Shell Model Grid: 128x8	Shell Model Grid: 160x10	Exact [24]
1	First flatwise bending	0.357	0.357	0.357	0.357
2	Second flatwise bending	2.236	2.236	2.236	2.237
3	First edgewise bending	5.009	5.009	4.989	5.048
4	First torsion	5.010	5.022	5.029	4.941
5	Third flatwise bending	6.252	6.258	6.258	6.264

Figure 5.3 illustrates first five mode shapes of shell model. The static analysis results of shell model for linear and nonlinear cases are given in structural model verifications in Chapter 5.2. The results are compared with the work of Castellani et al [33].

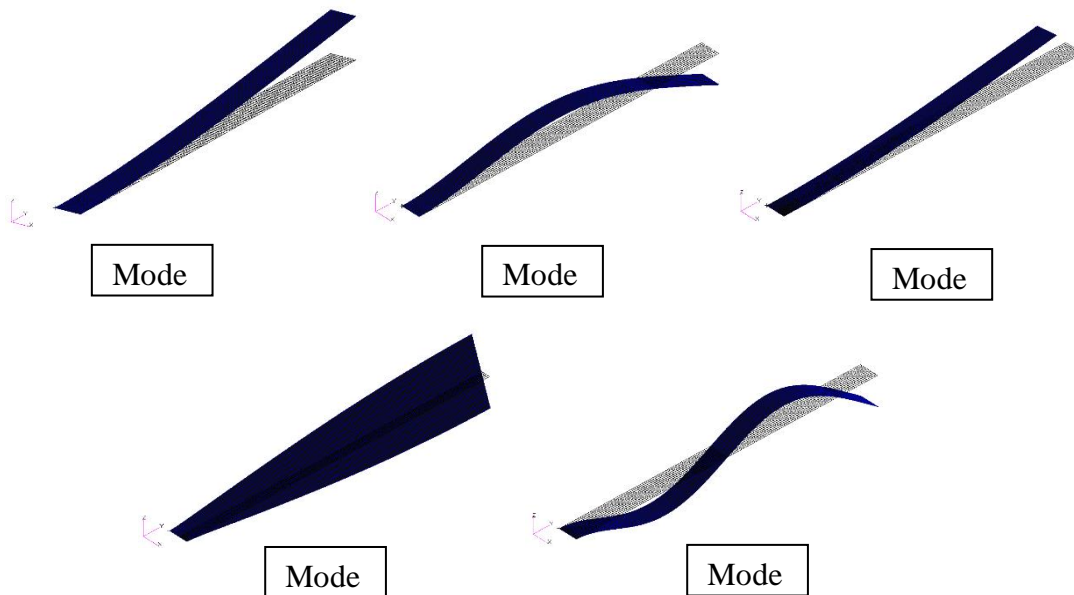


Figure 5.3. Mode shapes of the shell model

5.2. Structural Model Verifications

This section discusses the validation process of the analytical structural models. Before the construction of aeroelastic models, the structural models are verified with the given model in the literature; Patil-Hodges wing.

5.2.1. Bending-Torsion Beam FEM Verification

For the verification of the bending torsion beam finite element model, Patil-Hodges wing is used. Shell is modeled with MSC Nastran and verified with Castellani-Cooper results for the concentrated load case. Then, spanwise distributed load is applied to the shell model and bending-torsion beam finite element results are compared.

5.2.1.1. Concentrated Load Case

In the bending-torsion beam model, all degrees of freedom are uncoupled. For this reason, pure bending and torsion loading are applied individually. For the concentrated load case, vertical force and moment are applied at the tip location. In order to eliminate the differences between beam and shell model and to eliminate local effects, concentrated loads are applied as chordwise distributed loads as shown in Figure 5.4 and Figure 5.5.

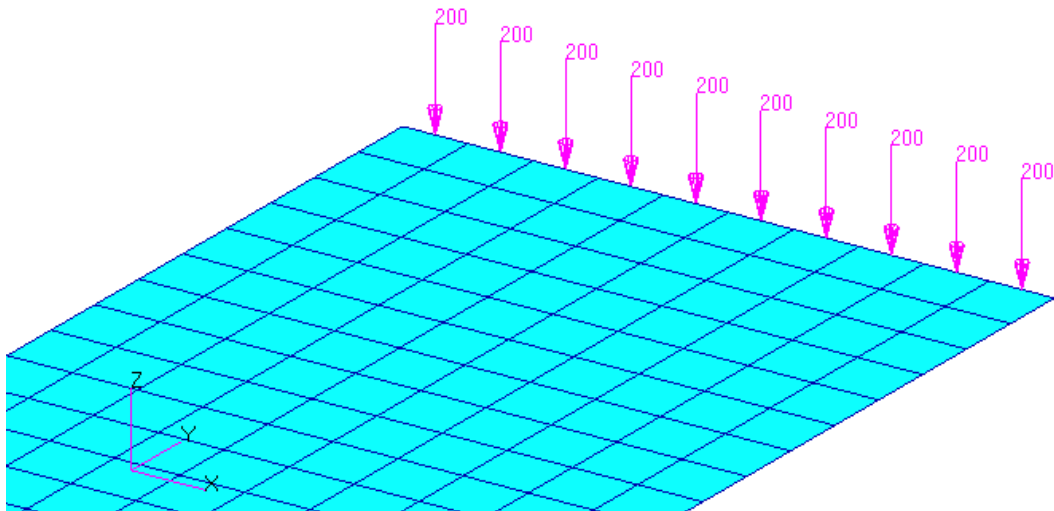


Figure 5.4. Vertical tip force application on the shell model

In Table 5.5, static analysis results of verified shell FE model is presented.

Table 5.5. Linear shell model verification for the vertical tip displacement: concentrated load case

Concentrated Vertical Tip Force [N]	<u>MSC Nastran Shell Model (Linear Static Analysis) 160x10 Elements</u>			<u>Castellani-Cooper Linear FEM</u>		
	25	100	200	25	100	200
Vertical Tip Displacement [m]	1.707	6.829	13.659	1.707	6.827	13.653

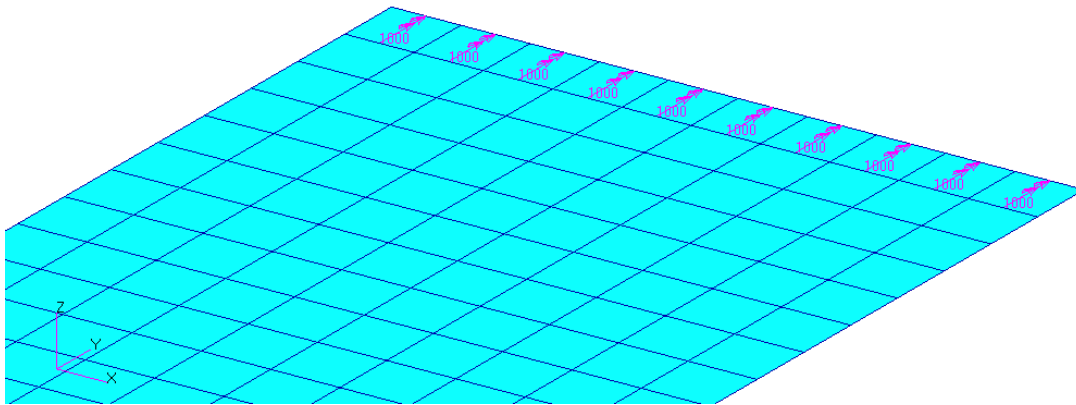


Figure 5.5. Pitching moment application at the tip location of the shell model

A mesh convergence study is implemented for bending-torsion beam FEM under concentrated vertical tip force and concentrated pitching moment. In Table 5.6, tip vertical displacement and bending rotation of bending-torsion beam FEM for varying element number under concentrated vertical tip force are demonstrated. The results of bending-torsion beam are compared with the static analysis results of MSC Nastran shell model. It is seen that element number has no significant effect on the static analysis results of the bending-torsion beam.

Table 5.6. *Bending-torsion beam structural model verification for the vertical displacement and bending rotation: concentrated load case*

	<u>Bending-Torsion Beam FEM 12 Elements</u>			<u>Bending-Torsion Beam FEM 24 Elements</u>			<u>MSC Nastran Shell Model (Linear Static Analysis) 160x10 Elements</u>		
	25	100	200	25	100	200	25	100	200
Concentrated Vertical Tip Force [N]									
Tip Vertical Displacement [m]	1.706	6.825	13.650	1.707	6.825	13.650	1.707	6.829	13.659
Tip Bending Rotation [rad]	0.160	0.640	1.280	0.160	0.640	1.280	0.160	0.640	1.280

In Table 5.7, tip twist angle results of the bending-torsion beam are compared with MSC Nastran shell model under concentrated pitching moment. It is seen that element number has no significant effect on the static analysis results of the bending-torsion beam.

Table 5.7. *Pitching moment vs elastic tip twist angle for the bending-torsion beam: concentrated load case*

	<u>Bending-Torsion Beam FEM 12 Elements</u>			<u>Bending-Torsion Beam FEM 24 Elements</u>			<u>MSC Nastran Shell Model (Linear Static Analysis) 160x10 Elements</u>		
	100	500	1000	100	500	1000	100	500	1000
Concentrated Pitching Moment [N × m]									
Tip Twist Angle [rad]	0.251	1.257	2.514	0.251	1.257	2.514	0.251	1.256	2.511

For pure vertical loading case and pure torsion case, the displacement results are similar for bending-torsion beam finite element model and MSC Nastran shell model.

5.2.1.2. Distributed Load Case

For the distributed load cases, vertical loading and torsion moment are applied along both the chordwise and spanwise direction, as shown in Figure 5.6 and Figure 5.7. Distributed load case verification is requisite to evaluate the consistent load vector calculation methodology of the developed FE models.

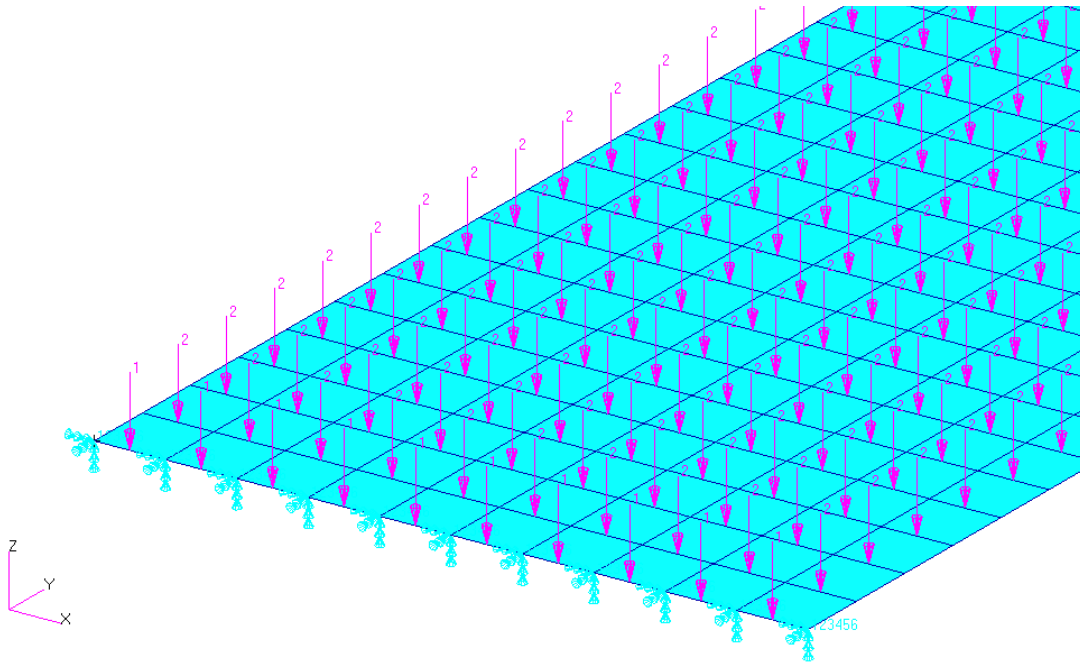


Figure 5.6. Distributed vertical load application on the shell model

In Table 5.8, the static analysis results of bending-torsion beam are compared with the static analysis results of MSC Nastran shell model under distributed vertical force. The tip displacement and tip bending rotation results of the bending-torsion beam FE model are nearly the same with the shell model.

Table 5.8. Pitching moment vs elastic tip twist angle for the bending-torsion beam: concentrated load case

Distributed Vertical Force [N/m]	<u>Bending-Torsion Beam FEM</u> 12 Elements			<u>MSC Nastran Shell Model</u> (<u>Linear Static Analysis</u>) 160x10 Elements		
	1	10	20	1	10	20
Tip Vertical Displacement [m]	0.410	4.095	8.190	0.410	4.100	8.197
Tip Bending Rotation [rad]	0.034	0.341	0.683	0.034	0.341	0.683

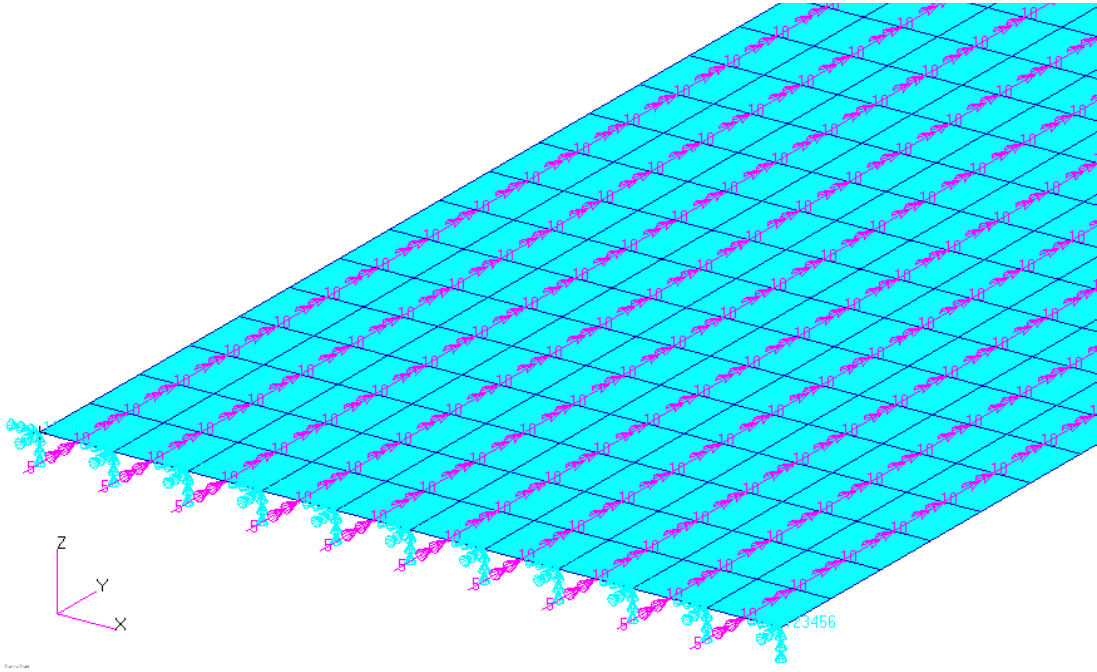


Figure 5.7. Distributed pitching moment application on the shell model

In Table 5.9, it is shown that for pure torsion load case, bending-torsion beam fem results are similar.

Table 5.9. Bending-torsion beam structural model verification for the elastic tip twist angle: distributed load case

	<u>Bending-Torsion Beam FEM 12 Elements</u>			<u>MSC Nastran Shell Model (Linear Static Analysis) 160x10 Elements</u>		
Distributed Pitching Moment [N]	10	50	100	10	50	100
Tip Twist Angle [rad]	0.201	1.006	2.011	0.195	0.973	1.945

5.2.2. Nonlinear Torsion Beam FEM Verification

For the verification of the nonlinear torsion beam finite element model Patil-Hodges and Trahair wing models are used. For the vertical displacements at the tip location,

wing is modeled with MSC Nastran shell model and verified with Castellani-Cooper results for the concentrated load case. For torsional twist at the tip location, MSC Nastran shell model results are verified for the concentrated load case. Then, distributed load is applied to the shell model of the wing model and nonlinear torsion beam FE results are compared.

5.2.2.1. Concentrated Load Case

In nonlinear torsion beam model, all degrees of freedom are uncoupled. For this reason, pure bending and torsion loading are applied individually. For the concentrated load case, chordwise distributed tip twisting moment is applied at the tip location. The load is applied as chord wisely distributed to eliminate the differences between beam and shell model and to eliminate local effects. In Table 5.10, MSC Nastran shell model is verified for the concentrated load case with the results of Cooper. Tip deflection results or nonlinear torsion beam FE model are compared with MSC shell model for concentrated and distributed load cases in Table 5.11 and Table 5.12, respectively.

Table 5.10. *Nonlinear shell model verification for the vertical tip displacement: concentrated load case*

Concentrated Vertical Tip Force [N]	<u>MSC Nastran Shell Model</u> (Nonlinear Static Analysis)			<u>Castellani-Cooper Nonlinear FEM</u>		
	25	100	200	25	100	200
Tip Vertical Displacement [m]	1.688	5.867	8.996	1.687	5.865	8.993

A mesh convergence study is implemented for nonlinear torsion beam FE model under concentrated load case. The results are compared with MSC Nastran shell model nonlinear static analysis results. From Table 5.11, it can be concluded that element number has no significant effects on the twist angle results.

Table 5.11. *Tip twist vs force for the nonlinear torsion beam: concentrated load case*

	<u>Nonlinear Torsion Beam FEM 12 Elements</u>			<u>Nonlinear Torsion Beam FEM 24 Elements</u>			<u>MSC Nastran Shell Model (Nonlinear Static Analysis)</u>		
	100	500	1000	100	500	1000	100	500	1000
Concentrated Pitching Moment [N]									
Tip Twist Angle [rad]	0.250	1.137	1.928	0.250	1.137	1.928	0.250	1.136	1.926

The nonlinear torsion beam fem results are similar with the shell model results for concentrated load case.

5.2.2.2. Distributed Load Case

For distributed load cases, torsion moment is applied spanwise direction. Distributed load case verification is requisite to evaluate consistent load vector application methodology. The nonlinear torsion beam fem results are similar with the shell model results for distributed load case.

Table 5.12. *Nonlinear torsion beam structural model verification for the tip twist angle: distributed load case*

	<u>Nonlinear Torsion Beam FEM</u>			<u>MSC Nastran Shell Model (Nonlinear Static Analysis)</u>		
	10	50	100	10	50	100
Distributed Twist Moment [N]						
Tip Twist Angle [rad]	0.200	0.898	1.604	0.194	0.878	1.585

5.3. Comparison of Structural Models

For the comparison of the structural models, spanwise vertical force and pitching moment is applied. Since the structural models do not contain coupled bending-torsion degrees of freedom, the loads are applied separately as pure bending and pure torsion.

5.3.1. Vertical Displacement Results Comparison of Structural Models

Table 5.13 reports the vertical displacement results of the structural models under spanwise distributed vertical load. It can be concluded that as the amount of force increases, the geometric nonlinearity becomes crucial.

Spanwise vertical displacement of the structural models, bending-torsion beam FE model and nonlinear torsion beam FE model, under variable loading can be seen from Figure 5.8, Figure 5.9 and Figure 5.10. As the magnitude of the loading increases, the difference between linear and nonlinear structural models grows. Bending-torsion beam model shows similar behavior with the linear static analysis results of MSC Nastran shell model.

Table 5.13. Vertical displacement vs force: distributed load case

Distributed Vertical Loading [N/m]	Tip Vertical Displacement [m]		
	<u>Bending-Torsion Beam FEM</u>	<u>MSC Nastran Shell Model (Linear Static Analysis)</u>	<u>MSC Nastran Shell Model (Nonlinear Static Analysis)</u>
1	0.410	0.410	0.410
10	4.095	4.100	3.902
20	8.190	8.197	6.925

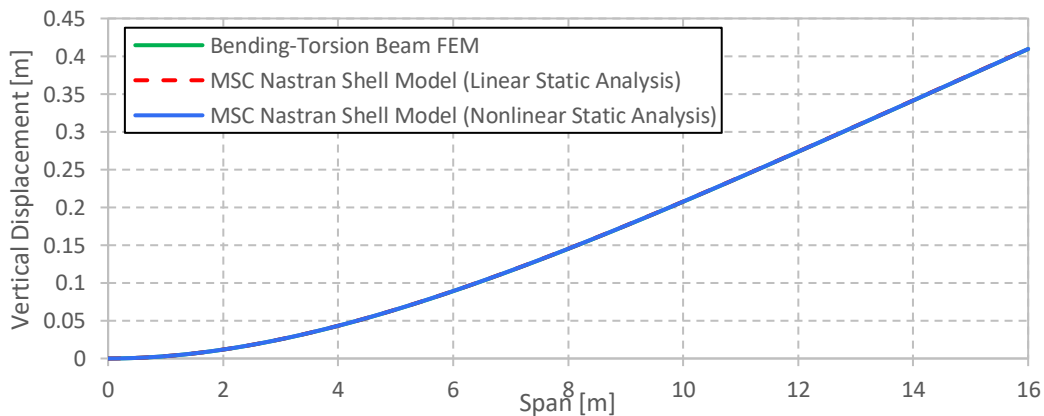


Figure 5.8. Spanwise vertical displacement of the wing: comparison of linear and nonlinear results under 1 N/m distributed vertical loading

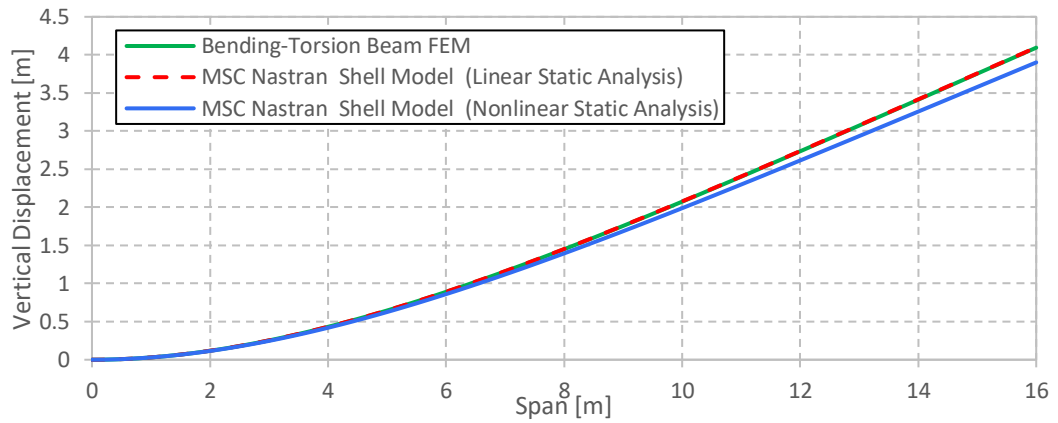


Figure 5.9. Spanwise vertical displacement of the wing: comparison of linear and nonlinear results under 10 N/m distributed vertical loading

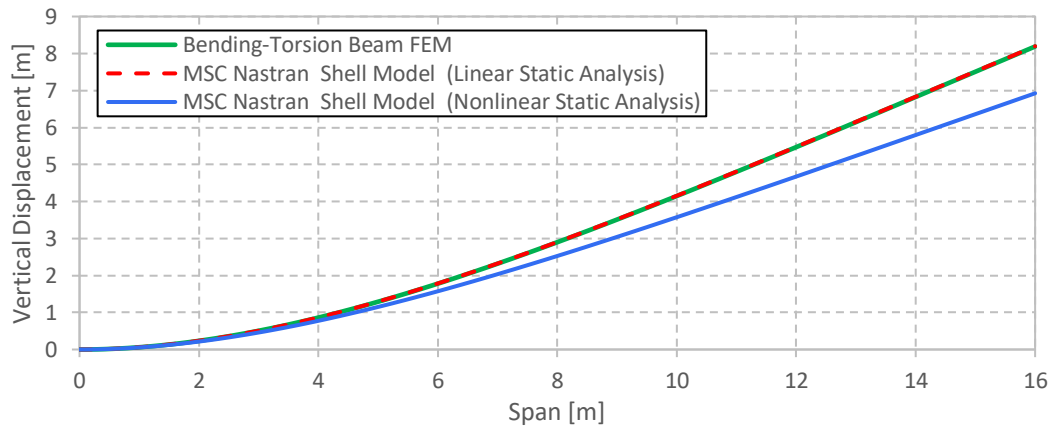


Figure 5.10. Spanwise vertical displacement of the wing: comparison of linear and nonlinear results under 20 N/m distributed vertical loading

5.3.2. Bending Rotation Angle Results Comparison of Structural Models

Table 5.14 reports the vertical displacement results of the structural models under spanwise distributed vertical load. The results obtained by different structural models are nearly the same.

Table 5.14. *Bending rotation vs force: distributed load case*

Distributed Vertical Loading, [N/m]	Tip Bending Rotation, [rad]		
	<u>Bending-Torsion Beam FEM</u>	<u>MSC Nastran Shell Model (Linear Static Analysis)</u>	<u>MSC Nastran Shell Model (Nonlinear Static Analysis)</u>
1	0.034	0.034	0.034
10	0.341	0.341	0.329
20	0.683	0.683	0.600

Figure 5.11, Figure 5.12 and Figure 5.13 indicate that linear structural model has similar spanwise bending rotation with MSC Nastran shell model. Nonlinear analysis results of MSC Nastran differ from the linear results as the amount of loading increases.

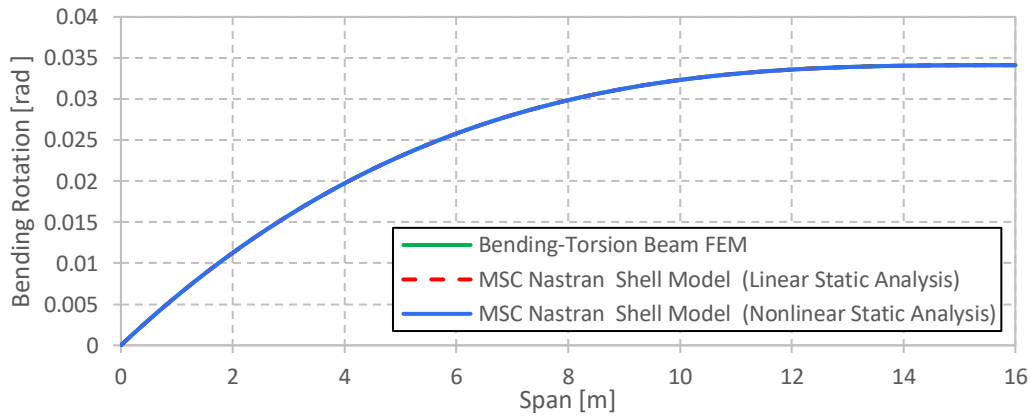


Figure 5.11. Spanwise bending rotation of the wing: comparison of linear and nonlinear results under 1 N/m distributed vertical loading

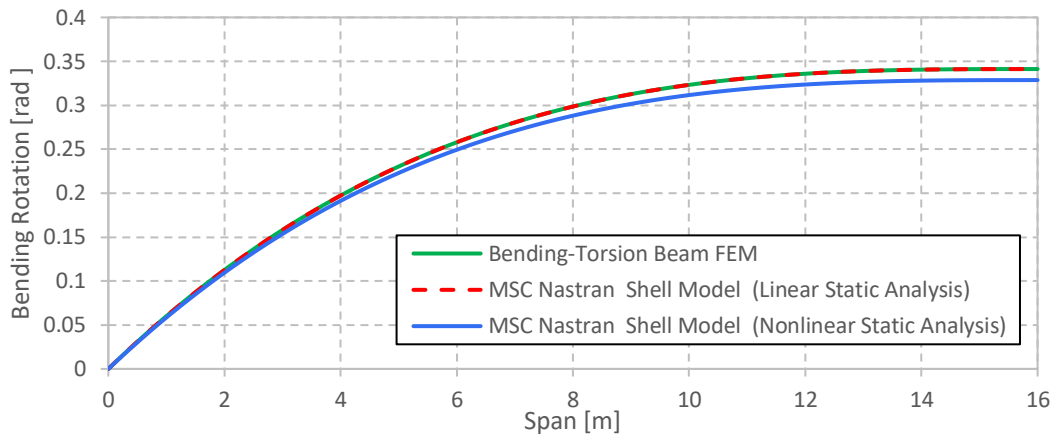


Figure 5.12. Spanwise bending rotation of the wing: comparison of linear and nonlinear results under 10 N/m distributed vertical loading

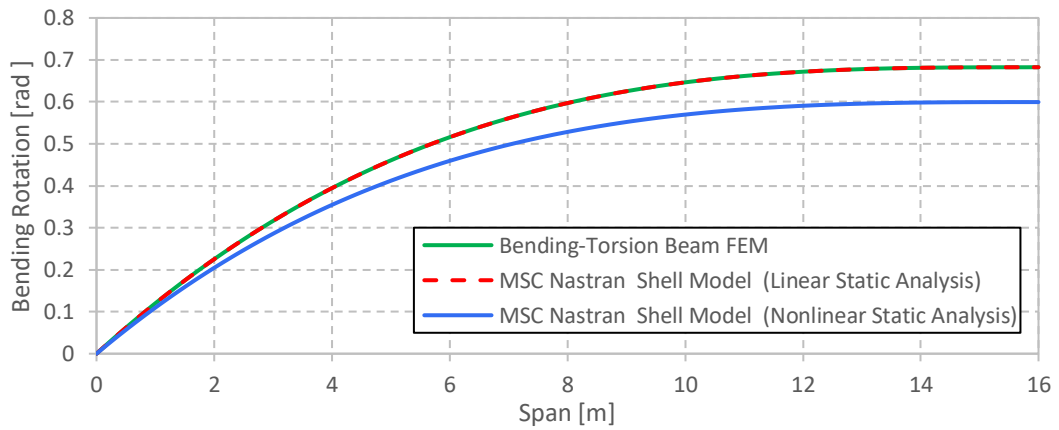


Figure 5.13. Spanwise bending rotation of the wing: comparison of linear and nonlinear results under 20 N/m distributed vertical loading

5.3.3. Twist Angle Results Comparison of Structural Models

Twist rotation of the structural models under distributed pitching moment are summarized in Table 5.15. The result of the developed FE models are closer to the results of MSC Nastran.

Table 5.15. Tip twist angle vs pitching moment: distributed load case

Distributed Pitching Moment [N]	Tip Twist Angle [rad]			
	<u>Bending-Torsion Beam FEM</u>	<u>MSC Nastran Shell Model (Linear Static Analysis)</u>	<u>Nonlinear Torsion Beam FEM</u>	<u>MSC Nastran Shell Model (Nonlinear Static Analysis)</u>
10	0.201	0.195	0.200	0.194
50	1.006	0.973	0.898	0.878
100	2.011	1.945	1.604	1.585

Figure 5.14, Figure 5.15 and Figure 5.16 indicate the spanwise twist rotation of structural models. The difference between linear and nonlinear models becomes larger as the amount of loading increases. Linear methods over-estimate the twist rotation. Linear analytical method has smaller twist rotation results than the linear MSC Nastran model. As the pitching moment increases, then the nonlinear torsion beam gives nearly the same results with the nonlinear Nastran model.

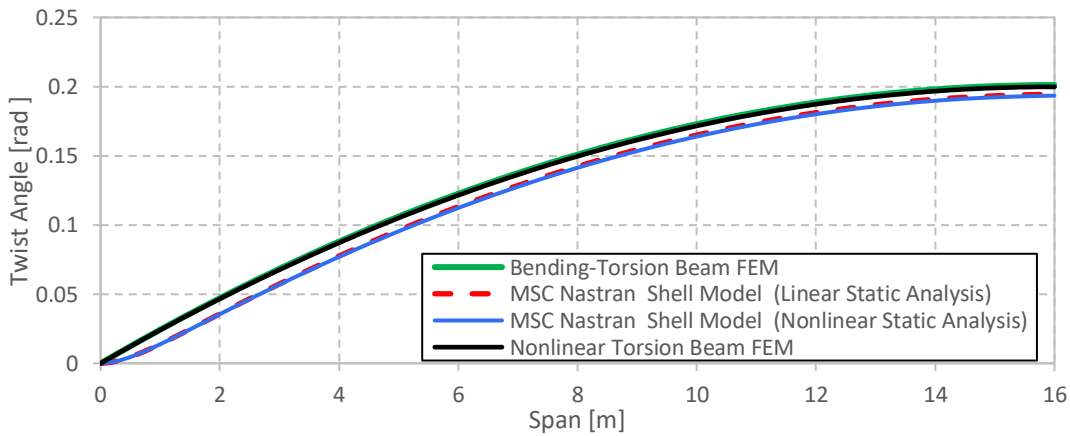


Figure 5.14. Spanwise twist rotation of the wing: comparison of linear and nonlinear results under 10 N distributed pitching moment

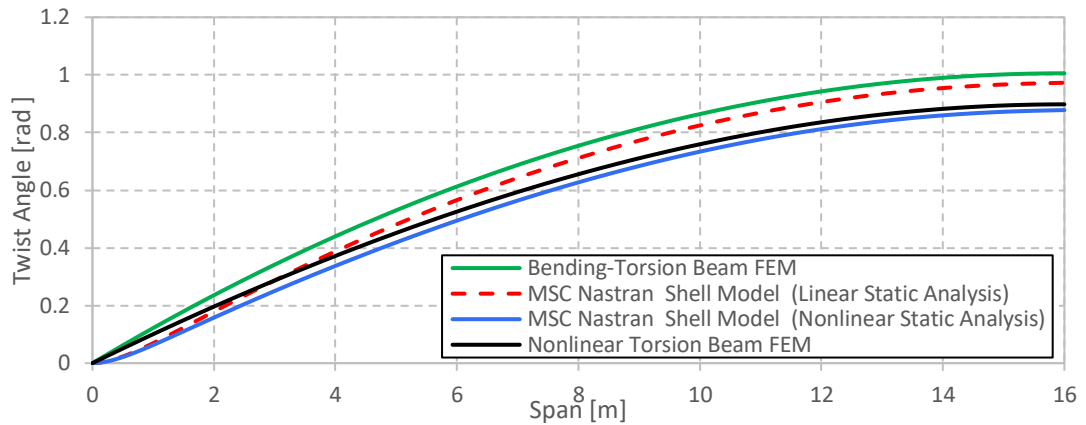


Figure 5.15. Spanwise twist rotation of the wing: comparison of linear and nonlinear results under 50 N distributed pitching moment

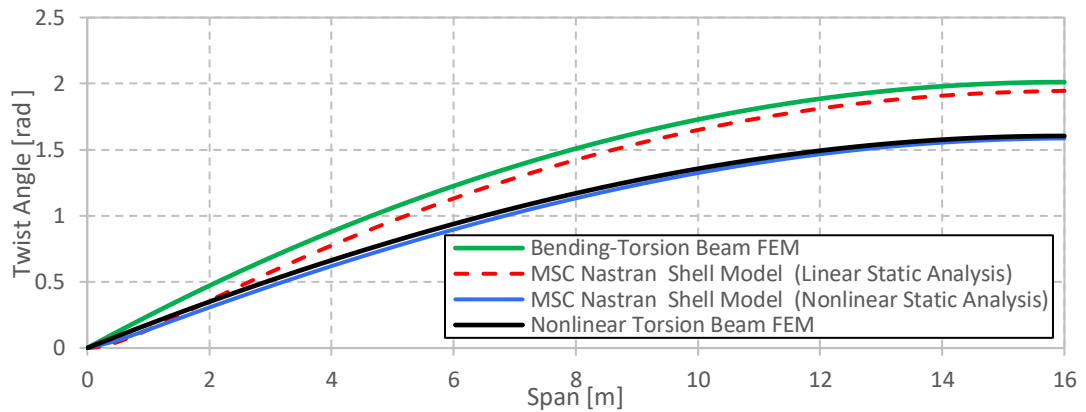


Figure 5.16 Spanwise twist rotation of the wing: comparison of linear and nonlinear results under 100 N distributed pitching moment

5.4. Comparison of Aeroelastic Models

Aeroelastic analyses are performed for low and high aspect ratio variations of the Patil-Hodges wing. The main aim is to investigate the geometric nonlinearity effect on the two different cases. For the high aspect-ratio model, structural models are coupled with the Strip Theory (lifting line theory). For low aspect-ratio model, both Strip Theory and lifting surface theory are preferred as an aerodynamic tool. Lifting surface theory is available for aspect ratio less than 12. The divergence analysis results

of the aeroelastic methods are discussed and compared. For the verification MSC Nastran trim analysis is performed.

5.4.1. Analysis of High Aspect Ratio Wings

Table 5.16 presents divergence analysis results of aeroelastic methods for the high aspect ratio wing model. Results are compared with the trim analysis results of MSC Nastran and linear aeroelastic result of the Patil-Hodges wing given in reference [24]. Linear methods give similar results as expected. However, all of them estimate conservative results. On the other hand, nonlinear method results in realistic divergence limit.

Table 5.16. *Comparison of divergence speed results of aeroelastic methods for high aspect ratio wing model*

Aeroelastic Method	Divergence Speed [m/s]
Method 1 : Bending-Torsion Beam FEM & Lifting Line Theory	39.43
Method 2: Nonlinear Torsion Beam FEM & Lifting Line Theory	55.72
MSC Nastran Trim Analysis of the Shell Model	37.54
Linear static aeroelastic analysis results of Patil et al. [24]	37.15

For the verification of nonlinear aeroelastic method, results of the developed FE model are compared with the graphical results of Cooper [33] in Figure 5.17. The spanwise elastic twist angle results of the linear and the nonlinear aeroelastic methods at 32.5 m/s. Analysis model of Cooper is the Patil-Hodges wing.

In Figure 5.17, linear result corresponds to linear FE method, NLFEM result corresponds to nonlinear FE method and MBD result corresponds to multibody dynamics.

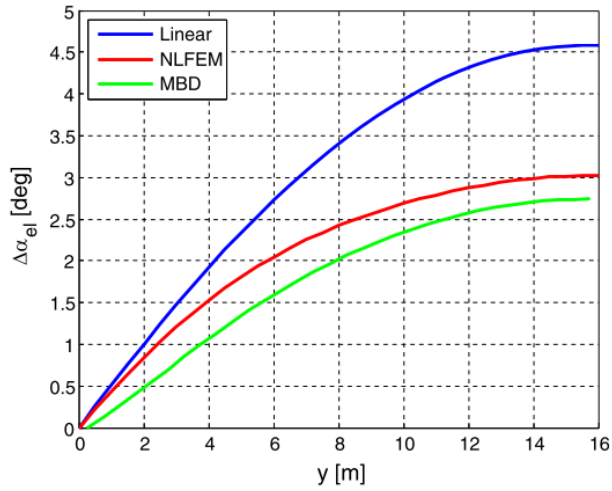


Figure 5.17 Elastic twist angle of Cooper's at 32.5m/s [33]

Comparing the local angle of attack along the span due to the wing elastic twist, it is clear that the twist predicted by the linear aeroelastic model (Method 1) is higher than the nonlinear model (Method 2) in Figure 5.18. The twist angle is underestimated in Figure 5.18 with respect to the results given in Figure 5.17.

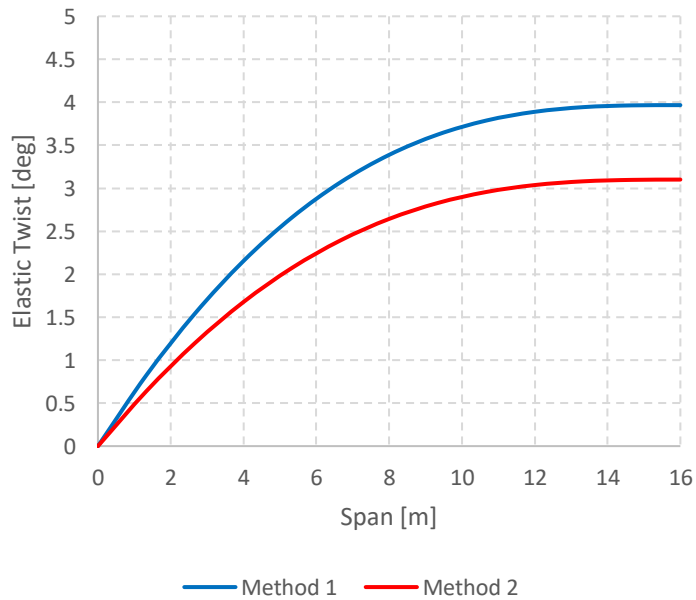


Figure 5.18 Elastic twist of developed FE models at 32.5m/s

5.4.2. Analysis of Low Aspect Ratio Wing Model

Lifting surface theory is suitable for aspect ratios less than 12; therefore, all the aeroelastic analysis are performed for the same Patil-Hodges wing (aspect ratio = 8). *Table 5.17* summarizes divergence speed results obtained by different methods. For the verification, MSC Nastran trim analysis of shell model is accomplished.

Table 5.17. Comparison of divergence speed results of aeroelastic methods for low aspect ratio wing model

Aeroelastic Method	Divergence Speed [m/s]
Method 1 : Bending-Torsion Beam FEM & Lifting Line Theory	192.55
Method 2 : Nonlinear Torsion Beam FEM & Lifting Line Theory	195.33
Method 3 : Bending-Torsion Beam FEM & Lifting Surface Theory	191.73
Method 4 : Nonlinear Torsion Beam FEM & Lifting Surface Theory	195.56
MSC Nastran Trim Analysis of the Shell Model	185.71

In Figure 5.19, stable aeroelastic deformations are given for the results of linear and nonlinear aeroelastic methods. Both the Method 1 and Method 2 are coupled with the lifting line theory. The tip twist angle is overestimated for these two methods. Method 3 and Method 4 are coupled with lifting surface theory. It can be deduced that the tip twist of the wing is close to zero when air speed V is close to 180 m/s when aerodynamic force equals gravity approximately for Method 3 and Method 4. The tip twist changes into nonlinear growth with the increase of air speed.

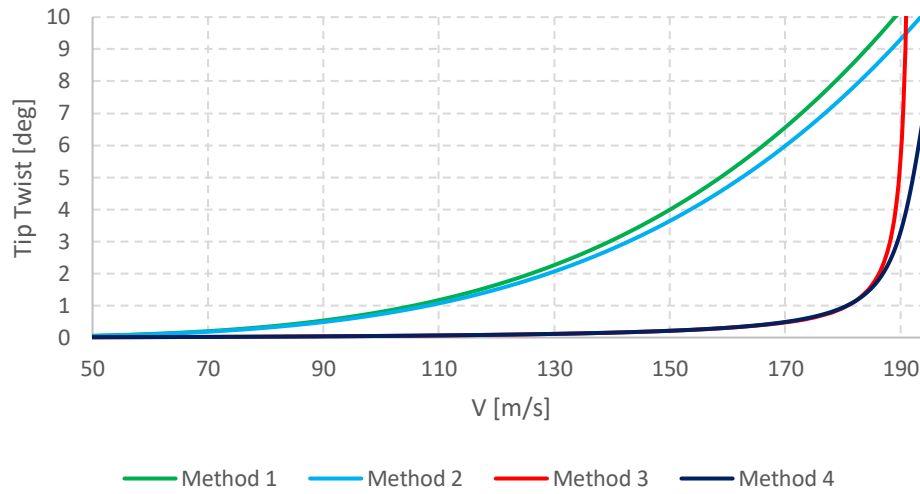


Figure 5.19 Comparison of linear and nonlinear method results of stable aeroelastic deformation

5.5. Case Studies

In this section, the sensitivity analyses are performed in order to see the effect of key parameters on the results. Key parameters are the aspect ratio of the wing, bending rigidity and torsion rigidity. Results are compared and discussed.

5.5.1. Aspect Ratio Effect on the Divergence Speed

Table 5.18 points out the importance of geometric nonlinearity for high aspect ratio wings. Method 1 is selected as a linear aeroelastic model and Method 3 is selected as a nonlinear aeroelastic model for the comparative study. Results indicate that for the low aspect ratio wings, linear aeroelastic methods are suitable, however regarding nonlinear effects is crucial for high aspect ratio wing with large geometrical deformation.

Table 5.18. Aspect ratio effect on the divergence speed

Aspect ratio	Divergence Speed [m/s]	
	Method 1	Method 3
8	192.55	195.33
32	39.43	55.72

5.5.2. Bending Rigidity Effect on the Divergence Speed

Table 5.19 represents the sensitivity of divergence speed with respect to bending rigidity. Method 1 is selected as an analysis model for the comparative study. The change in EI has no effect upon divergence speed due to the uncoupled degrees of freedom, as expected.

Table 5.19. *Sensitivity of divergence speed with respect to EI*

EI [Nm ²]	GJ [Nm ²]	Divergence Speed [m/s]
1.5×10^4	0.636×10^4	39.43
2×10^4	0.636×10^4	39.43
2.5×10^4	0.636×10^4	39.43

5.5.3. Torsional Rigidity Effect on the Divergence Speed

Table 5.20 represents the sensitivity of divergence speed with respect to torsional rigidity. Method 1 is selected as an analysis model for the comparative study. Varying GJ has a great influence on the divergence speed which is very sensitive in GJ.

Table 5.20. *Sensitivity of divergence speed with respect to GJ*

EI [Nm ²]	GJ [Nm ²]	Divergence Speed [m/s]
2×10^4	0.477×10^4	31.17
2×10^4	0.636×10^4	39.43
2×10^4	0.954×10^4	48.52

CHAPTER 6

CONCLUSION

The aim of this thesis is to examine static aeroelastic analysis of high aspect ratio wings utilizing different fidelity structural models for the preliminary design stage of the aircraft. Structural models are based on linear and nonlinear theories. The linear structural model is the bending-torsion beam finite element model. The nonlinear structural model is based on nonlinear torsion finite element method. Aerodynamic models are the lifting line theory and the lifting surface theory. Validation studies are established to confirm the accuracy of structural and aeroelastic methodologies. For the verification, MSC Nastran trim solution is preferred.

This thesis is mainly focused on the preliminary design phase with the implementation of simple models and it presents an efficient and practical perspective to the linear and nonlinear static aeroelastic solution methodologies. Without the three-dimensional wing model or the finite element model of the wing, aeroelastic behavior at the trim condition can be predicted and divergence speed can be obtained.

As the analysis model, the Patil-Hodges wing which is frequently referred to in the literature is preferred. Before the construction of aeroelastic models, the structural models are verified under concentrated and distributed loadings. For the comparison of the structural models, spanwise vertical force and pitching moment is applied. The difference between linear and nonlinear models become larger as the amount of loading increases.

Aeroelastic analyses are performed for low and high aspect ratio variations of Patil-Hodges wing. The main aim is to investigate the geometric nonlinearity effect on the two different cases. For the high aspect-ratio model, structural models are coupled with lifting line theory. For the low aspect-ratio model, both the lifting line theory and

the lifting surface theory are preferred as an aerodynamic tool since lifting surface theory is available for aspect ratio is less than 12.

Bending-torsion beam depends on finite element analysis hence it is convenient for variable cross-sections. Nonlinear torsion beam relies on nonlinear finite element procedure. It is suitable for both the variable cross-sections and high aspect ratio wings. Linear structural modeling is found to be conservative for high aspect ratio. Geometric nonlinearity is appropriate for highly deformable structures and appropriate to prevent over safe designs.

For the further investigation, bending-torsion degrees of freedom can be coupled to see the effect of bending on the divergence speed. Nonlinearity can be modeled not only for torsional degrees of freedom but also for the bending rotation. In addition, aeroelastic solutions can also be expanded for time dependency in order to analyze geometric nonlinearity effect on the flutter speed. Further case studies can be performed for taper ratio and sweep angle. Moreover, nonlinear aerodynamic solver can be preferred.

REFERENCES

- [1] D. H. Hodges and G. A. Pierce, "Introduction to Structural Dynamics and Aeroelasticity." pp. 1–181, 2006.
- [2] E. H. Dowell, *A Modern Course in Aeroelasticity*, vol. 217. 2015.
- [3] A. R. Collar, "The First Fifty Years of Aeroelasticity," *Aerospace*, vol. 5. pp. 12–20, 1978.
- [4] P. P. Friedmann, "Renaissance of Aeroelasticity and Its Future," *J. Aircr.*, vol. 36, no. 1, pp. 105–121, 1999.
- [5] E. H. Dowell and K. C. Hall, "Mathematical Modeling of Fluid-structure Interaction," *Annu. Rev. Fluid Mech.*, vol. 33, no. 1, pp. 445–490, 2001.
- [6] E. Livne, "Future of Airplane Aeroelasticity," *J. Aircr.*, vol. 40, no. 6, pp. 1066–1092, 2003.
- [7] O. O. Bendiksen, "Modern Developments in Computational Aeroelasticity," *Proc. Inst. Mech. Eng. Part G J. Aerosp. Eng.*, vol. 218, no. 3, pp. 157–177, 2004.
- [8] E. Livne and T. A. Weisshaar, "Aeroelasticity of Nonconventional Airplane Configurations-Past and Future," *J. Aircr.*, vol. 40, no. 6, pp. 1047–1065, 2003.
- [9] D. M. Schuster, D. D. Liu, and L. J. Huttshell, "Computational Aeroelasticity: Success, Progress, Challenge," *J. Aircr.*, vol. 40, no. 5, pp. 843–856, 2003.
- [10] K. G. Bhatia, "Airplane Aeroelasticity: Practice and Potential," *J. Aircr.*, vol. 40, no. 6, pp. 1010–1018, 2008.
- [11] J. Xiang, Y. Yan, and D. Li, "Recent Advance in Nonlinear Aeroelastic Analysis and Control of the Aircraft," *Chinese J. Aeronaut.*, vol. 27, no. 1, pp. 12–22, 2014.

- [12] F. Afonso, J. Vale, É. Oliveira, F. Lau, and A. Suleman, “A Review on Non-Linear Aeroelasticity of High Aspect-Ratio Wings,” *Prog. Aerosp. Sci.*, vol. 89, no. August 2016, pp. 40–57, 2017.
- [13] T. Quackenbush, J. Keller, A. Boschitsch, G. Whitehouse, and R. McKillip, “Modeling Tools for Real Time Aeroservoelastic Simulation with Nonlinear Aerodynamics,” no. August, pp. 1–18, 2009.
- [14] M. J. De *et al.*, “Non-linear aeroelastic prediction for aircraft applications,” *Prog. Aerosp. Sci.*, vol. 43, no. 4–6, pp. 65–137, 2007.
- [15] Y. Bazilevs, K. Takizawa, and T. E. Tezduyar, *Computational Fluid Structure Interaction*, 1st ed. Chichester: Wiley & Sons Ltd, 2013.
- [16] R. Kamakoti and W. Shyy, “Fluid-structure interaction for aeroelastic applications,” *Prog. Aerosp. Sci.*, vol. 40, no. 8, pp. 535–558, 2004.
- [17] B. Hallissy and C. Cesnik, “High-fidelity Aeroelastic Analysis of Very Flexible Aircraft,” no. April, 2014.
- [18] H. H. Mian, G. Wang, and Z. Y. Ye, “Numerical investigation of structural geometric nonlinearity effect in high-aspect-ratio wing using CFD/CSD coupled approach,” *J. Fluids Struct.*, vol. 49, pp. 186–201, 2014.
- [19] D. Tang and E. H. Dowell, “Experimental and Theoretical Study on Aeroelastic Response of High-Aspect-Ratio Wings,” *AIAA J.*, vol. 39, no. 8, pp. 1430–1441, 2001.
- [20] P. DUNN and J. DUGUNDJI, “Nonlinear stall flutter and divergence analysis of cantilevered graphite/epoxy wings,” *AIAA J.*, vol. 30, no. 1, pp. 153–162, 1992.
- [21] M. J. Patil, D. H. Hodges, and C. E. S. Cesnik, “Characterizing the Effects of Geometrical Nonlinearities on Aeroelastic Behavior of High-Aspect-Ratio Wings,” *Int. Forum Aeroelasticity Struct. Dyn.*, no. August 2014, pp. 1–10,

1999.

- [22] M. J. Patil and D. H. Hodges, “Nonlinear Aeroelastic Analysis of Complete Aircraft in Subsonic Flow,” *J. Aircr.*, vol. 37, no. 5, pp. 753–760, 2000.
- [23] M. Goland, “The Flutter of a Uniform Cantilever Wing,” *J. Appl. Mech. Asme*, pp. A197–A208, 1945.
- [24] M. J. Patil, D. H. Hodges, and C. E. S. Cesnik, “Nonlinear Aeroelasticity and Flight Dynamics of High-Altitude Long-Endurance Aircraft,” *J. Aircr.*, vol. 38, no. 1, pp. 88–94, 2001.
- [25] M. J. Patil and D. H. Hodges, “On the Importance of Aerodynamic and Structural Geometrical Nonlinearities in Aeroelastic Behavior of High-Aspect-Ratio Wings,” *J. Fluids Struct.*, vol. 19, no. 7, pp. 905–915, 2004.
- [26] C. C. Xie, J. Z. Leng, and C. Yang, “Geometrical Nonlinear Aeroelastic Stability Analysis of a Composite High-Aspect-Ratio Wing,” *Shock Vib.*, vol. 15, no. 3–4, pp. 325–333, 2008.
- [27] D. Tang, A. Grash, and E. H. Dowell, “Gust Response for Flexibly Suspended High-Aspect Ratio Wings,” *AIAA J.*, vol. 48, no. 10, pp. 2430–2444, 2010.
- [28] C. C. Xie, Y. Liu, and C. Yang, “Theoretic analysis and experiment on aeroelasticity of very flexible wing,” *Sci. China Technol. Sci.*, vol. 55, no. 9, pp. 2489–2500, 2012.
- [29] M. Y. Harmin and J. E. Cooper, “Aeroelastic Behaviour of a Wing Including Geometric Nonlinearities,” *Aeronaut. J.*, vol. 115, no. 1174, pp. 767–777, 2011.
- [30] M. I. McEwan, J. R. Wright, J. E. Cooper, and A. Y. T. Leung, “A Combined Modal/Finite Element Analysis Technique for The Dynamic Response of a Non-Linear Beam to Harmonic Excitation,” *J. Sound Vib.*, vol. 243, no. 4, pp. 601–624, 2001.
- [31] D. Huixue, Y. Zhichun, and L. Yi, “Accelerated Loosely-Coupled CFD/CSD

- Method for Nonlinear Static Aeroelasticity Analysis,” *Aerosp. Sci. Technol.*, vol. 14, no. 4, pp. 250–258, 2010.
- [32] C. Howcroft *et al.*, “Aeroelastic Modelling of Highly Flexible Wings,” *15th Dyn. Spec. Conf.*, 2016.
- [33] M. Castellani, J. E. Cooper, and Y. Lemmens, “Nonlinear Static Aeroelasticity of High-Aspect-Ratio-Wing Aircraft by Finite Element and Multibody Methods,” *J. Aircr.*, vol. 54, no. 2, pp. 548–560, 2017.
- [34] Y. Lan, X. Changchuan, Y. Chao, Z. Bing, and A. Da Rouch, “Nonlinear Static Aeroelastic Analysis of High- Aspect Ratio Wing Based on CFD/CSD Coupling Solution,” *Ifasd*, no. June, pp. 1–13, 2017.
- [35] C. Xie, C. An, Y. Liu, and C. Yang, “Static Aeroelastic Analysis Including Geometric Nonlinearities Based on Reduced Order Model,” *Chinese J. Aeronaut.*, vol. 30, no. 2, pp. 638–650, 2017.
- [36] C. Zhang, Z. Zhou, X. Zhu, and P. Meng, “Nonlinear Static Aeroelastic and Trim Analysis of Highly Flexible Joined-Wing Aircraft,” *AIAA J.*, vol. 56, no. 12, pp. 4988–4999, 2018.
- [37] E. Kantor, D. E. Raveh, and R. Cavallaro, “Nonlinear Structural, Nonlinear Aerodynamic Model for Static Aeroelastic Problems,” *AIAA J.*, vol. 57, no. 5, pp. 2158–2170, 2019.
- [38] B. Sümer, “Fluid Structure Coupled Analysis of an Aerodynamic Surface,” Middle East Technical University, 2004.
- [39] U. Susuz, “Aeroelastic Analysis of An Unmanned Aerial Vehicle,” Middle East Technical University, 2008.
- [40] E. Başkut, “Development of a Closely Coupled Approach for Solution of Static and Dynamic Aeroelastic Problems,” Middle East Technical University, 2010.
- [41] O. Dababneh, “Design, Analysis and Optimization of Thin Walled Semi-

- Monocoque Wing Structures Using Different Structural Idealizations in The Preliminary Design Phase,” Middle East Technical University.
- [42] L. Ünlüsoy, “Effects of Morphing on Aeroelastic Behavior of Unmanned Aerial Vehicle Wings,” 2014.
- [43] E. Ünay, “Load Analysis of an Aircraft Using Simplified Aerodynamic,” Middle East Technical University, 2015.
- [44] Ö. Özkaya, “Nonlinear Static Aeroelastic Behavior of Composite Missile Fin with Interlaminar and Intralaminar Damage,” Middle East Technical University, 2017.
- [45] J. R. Wright and J. E. Cooper, *Introduction to Aircraft Aeroelasticity and Loads*, Second. John Wiley & Sons, Ltd Registered, 2015.
- [46] Y. C. Fung, *An Introduction to the Theory of Aeroelasticity*. New York: Dover Publications, Inc.
- [47] The Royal Aeronautical Society, “ESDU 95010 - Computer Program for Estimation of Spanwise Loading of Wings with Camber and Twist in Subsonic Attached Flow,” vol. 1999, no. June 1995. 1999.
- [48] H. Multhopp, “Methods for Calculating the Lift Distribution of Wings (Subsonic Lifting-Surface Theory),” *Aeronaut. Res. Council.*, vol. 2884, no. 2884, 1950.
- [49] NX and Nastran, “Aeroelastic Analysis User’s Guide.” Siemens Product Lifecycle Management Software Inc., 2014.
- [50] “MSC.FlightLoads and Dynamics User’s Guide Version 2006.” MSC.Software Corporation, 2006.
- [51] K. J. Bathe, *Finite Element Procedure*, 2nd ed. New Jersey: Prentice Hall, 1996.
- [52] R. D. Cook, D. S. Malkus, and M. E. Plesha, *Concepts and Applications of*

Finite Element Analysis. 1989.

- [53] F. P. Beer, E. R. Johnston, Jr., J. T. DeWolf, and D. F. Mazurek, *Mechanics of Materials*, 6th ed. New York: McGraw-Hill, 2012.
- [54] N. Kim, *Introduction to Nonlinear Finite Element Analysis*. 2015.
- [55] G. Chen and N. S. Trahair, “Inelastic Nonuniform Torsion of Steel I-Beams,” vol. 23, no. 1992, pp. 189–207, 2006.
- [56] N. S. Trahair and S. Bild, “Elastic Biaxial Bending and Torsion of Thin-Walled Members,” *Thin-Walled Struct.*, vol. 9, no. 1–4, pp. 269–307, 1990.
- [57] A. Billinghamurst, J. R. L. Williams, G. Chen, and N. S. Trahair, “Inelastic uniform torsion of steel members,” *Comput. Struct.*, vol. 42, no. 6, pp. 887–894, 1992.
- [58] S. Timoshenko and J. N. Goodier, *Theory of Elasticity*, 1st ed. New York: McGraw-Hill, 1951.
- [59] N. S. Trahair, “Nonlinear Elastic Nonuniform Torsion,” *J. Struct. Eng.*, vol. 131, no. 7, pp. 1135–1142, 2005.
- [60] N. S. Trahair, “Flexural-torsional buckling of structures,” *New directions in civil engineering*. p. 360, 1993.
- [61] M. J. Patil, D. H. Hodges, and C. E. S. Cesnik, “Limit Cycle Oscillation of High-Aspect-Ratio Wings,” *Appl. Mech. Mater.*, vol. 556–562, no. c, pp. 4329–4332, 1999.

